

Observation of a charge-neutral muon-polaron complex in antiferromagnetic Cr_2O_3

M. H. Dehn,^{1,2,3,*} J. K. Shenton,⁴ S. Hohenstein,^{5,6} Q. N. Meier,⁴ D. J. Arseneau,³ D. L. Cortie,^{1,2,7,†} B. Hitti,³ A. C. Y. Fang,^{1,‡} W. A. MacFarlane,^{2,3,7} R. M. L. McFadden,^{2,7} G. D. Morris,³ Z. Salman,⁶ H. Luetkens,⁶ N. A. Spaldin,⁴ M. Fechner,^{4,8} and R. F. Kiefl^{1,2,3}

¹*Department of Physics and Astronomy, University of British Columbia, Vancouver, BC V6T 1Z1, Canada*
²*Stewart Blusson Quantum Matter Institute, University of British Columbia, Vancouver, BC V6T 1Z4, Canada*

³TRIUMF, Vancouver, BC V6T 2A3, Canada

⁴*Department of Materials, ETH Zürich, CH-8093 Zürich, Switzerland*

⁵*Physik-Institut der Universität Zürich, CH-8057, Zürich, Switzerland*

⁶*Laboratory for Muon Spin Spectroscopy, Paul Scherrer Institut, 5232, Villigen PSI, Switzerland*

⁷*Department of Chemistry, University of British Columbia, Vancouver, BC, V6T 1Z1, Canada*

⁸*Max Planck Institute for the Structure and Dynamics of Matter, 22761 Hamburg, Germany*

(Dated: September 4, 2019)

We report a comprehensive muon spin rotation (μSR) study of the prototypical magnetoelectric antiferromagnet Cr_2O_3 . We find the positively charged muon (μ^+) occupies several distinct interstitial sites, and displays a rich dynamic behavior involving local hopping, thermally activated site transitions and the formation of a charge-neutral complex composed of a muon and an electron polaron. The discovery of such a complex has implications for the interpretation of μSR spectra in a wide range of magnetic oxides, and opens a route to study the dopant characteristics of interstitial hydrogen impurities in such materials. We address implications arising from implanting a μ^+ into a linear magnetoelectric, and discuss the challenges of observing a local magnetoelectric effect generated by the charge of the muon.

I. INTRODUCTION

Positively charged muons implanted into semiconductors and insulators often form muonium ($\text{Mu} = [\mu^+e^-]$), a hydrogen-like charge-neutral bound state. It is conventionally referred to as a *paramagnetic* center as the bound electron is unpaired and its spin is decoupled from all the other electrons. Since the electronic structure of Mu in a solid is virtually identical to that of hydrogen, Mu has been studied extensively using muon spin spectroscopy (μSR) to learn about interstitial hydrogen, one of the most ubiquitous defects in semiconductors. In a μSR experiment, spin polarized muons (μ^+) are implanted into the sample of interest and the subsequent time evolution of the spin polarization is observed, providing an accurate measurement of the magnetic coupling of the muon spin with its environment [1]. Mu centers have been studied in a wide range of materials, providing direct information about the electronic structure of hydrogen defects as shallow or deep-level dopants [2–5]. So far, the study of such charge-neutral muon states has been limited to non-magnetic materials, since paramagnetic Mu is widely assumed to be subject to strong depolarization in the presence of magnetic moments such as those on Cr^{3+} [3], and, with the exception of MnF_2 [6], no Mu has been confirmed in magnetic materials.

Here, we present strong evidence for a charge-neutral muon state in the antiferromagnet Cr_2O_3 . In particular, our data, in conjunction with detailed density functional theory (DFT) calculations, make a compelling case for the existence of a muon-polaron complex, where the positive muon is bound to an oxygen and an excess electron localizes on a nearby Cr ion, changing its valence to Cr^{2+} ($3d^4$). The degeneracy of the now occupied e_g orbital is lifted via a lattice distortion, leading to a Jahn-Teller (JT) polaron [7–9] on the Cr ion. Crucially, the resulting JT-stabilized muon-polaron complex is *not paramagnetic* and therefore *distinct from Mu*, since the bound electron is strongly coupled to the $3d$ electrons of the Cr host ion. Therefore, no signatures conventionally associated with a charge-neutral state are displayed, concealing its existence. However, in spite of its inconspicuous signal, the presence of such a complex has a significant impact on the location and stability of muon stopping sites, and the local fields experienced there.

This discovery of a charge-neutral muon-polaron complex in Cr_2O_3 suggests that neutral charge states could form in other insulating magnetic materials as well, which has implications for the interpretation of a wide range of μSR data. Furthermore, analogous to Mu in semiconductors, the study of muon-polaron complexes in magnetic oxides may provide detailed information on the dopant characteristics of interstitial hydrogen, a good understanding of which is crucial for a precise control of charge carriers in such materials.

Cr_2O_3 is of additional interest due to its magnetoelectric properties. Being the first material predicted [10] and measured [11, 12] to exhibit an induced linear polarization (magnetization) in response to a magnetic (electric) field, it is widely regarded as *the* prototypical linear mag-

* mdehn@triumf.ca

† Present address: Institute for Superconducting and Electronic Materials, Australian Institute for Innovative Materials, University of Wollongong, North Wollongong, NSW 2500, Australia

‡ Present address: Department of Physics, Simon Fraser University, Burnaby, Canada V5A 1S6

netoelectric [13, 14] and remains the subject of active research [15], directed primarily at exploiting its magneto-electric properties for device applications [16–18]. In addition, there are unresolved fundamental questions raised by the recent prediction that an electric charge within a linear magnetoelectric is surrounded by a monopolar magnetic field distribution, and thus is subject to a magnetic force in an external magnetic field [19]. μ SR is a unique way to investigate such predictions since the spin polarized muon acts both as a test charge and a sensitive probe of the local magnetic field. However, as indicated by studies from the early days of μ SR [20–23], the spectra in Cr_2O_3 are complex and their interpretation was inconclusive. Furthermore, given the weak magnetoelectric coupling in Cr_2O_3 , only subtle changes to the local magnetic environment in response to the muon charge are expected, and a thorough understanding of the interaction between the implanted muon and host material is required as a prerequisite for the search for any muon-induced magnetoelectric effects.

The paper proceeds as follows. In Sec. II, we briefly introduce the μ SR technique and summarize the experimental conditions. Next, in Sec. III, we report the results of a comprehensive μ SR study of Cr_2O_3 under zero-field conditions and in applied magnetic fields. The data are presented in three parts: (1) In zero field, up to three spin precession frequencies are observed, indicating three distinct muon environments with different internal magnetic fields \mathbf{B}_{int} . (2) Weak external fields $\mathbf{B}_{ext} (\ll \mathbf{B}_{int})$ split the observed frequencies into multiplets, providing detailed information on the orientation of the internal fields. (3) Large applied fields ($\mathbf{B}_{ext} > \mathbf{B}_{int}$) corroborate the weak field results and reveal an additional frequency. Together, the data exhibit a rich variety of dynamic phenomena that we explain in terms of site metastability and muon dynamics (Sec. IV). Most importantly, above ~ 150 K, we observe both highly dynamic muons undergoing locally restricted hopping and muons that remain static in their site. In order to explain this surprising behavior, we turn to DFT to identify candidate muon sites for all three environments, and conclude that the coexistence of site-stable and dynamic muons can be explained with the formation of a charge-neutral Jahn-Teller-stabilized muon-polaron complex (Sec. V). Finally, in Sec. VI, we discuss the implications of charge-neutral states in Cr_2O_3 and its relevance for other magnetic oxides, and possible consequences arising from implanting positively charged muons into a linear magnetoelectric.

II. EXPERIMENTAL DETAILS

The μ SR experiments reported on here were carried out at the Centre for Molecular and Materials Science at TRIUMF (Vancouver, Canada), although initial spectra were taken at the GPS instrument at PSI (Villigen, Switzerland). The zero and low magnetic field measure-

ments were taken in the LAMPF spectrometer and the high magnetic field data were acquired in the NuTime spectrometer. All data were acquired with the initial muon spin polarization \mathbf{P}_i perpendicular to the beam direction (\hat{z}).

In a μ SR experiment, spin polarized, positively charged muons are implanted into the sample, where they decay with a lifetime of $\tau_\mu = 2.2 \mu\text{s}$. The resulting decay positron is emitted preferentially along the muon spin direction, and can be detected in a time-resolved manner with plastic scintillators placed in pairs around the sample. This anisotropic positron emission introduces a spin-dependent imbalance in the count rate, causing the asymmetry signal $S(t)$, the count-normalized difference of a counter pair, to be directly proportional to the spin polarization $P(t)$ along the detector axis. A detailed description of the μ SR technique can be found in Ref. 1. In the presence of a magnetic field \mathbf{B} , the muon spin precesses about the field direction with frequency $f = \gamma_\mu/2\pi \cdot |\mathbf{B}|$, where $\gamma_\mu = 2\pi \cdot 0.01355 \text{ MHz/G}$ is the muon gyromagnetic ratio. This allows for a direct measure of the local magnetic field experienced by the muon.

In a crystal lattice, the charged muon usually stops in one or more distinct sites that minimize the overall energy. At a given temperature, several crystallographically distinct sites may be populated, each of which causes a different time evolution of the spin polarization. For example in magnetic materials, muons may experience different internal fields at inequivalent sites, causing spin precession at different frequencies. In this case, the observed signal $S(t)$ is a sum of several components $S_i(t)$. In this paper, oscillatory signals are fit to exponentially damped cosines

$$S_i(t) = A_i \cos(2\pi f_i t + \phi_i) \exp(-\lambda_i t), \quad (1)$$

where the amplitude A_i is a measure of the signal weight, f_i is the frequency, ϕ_i the initial phase, and λ_i the relaxation rate. Non-oscillatory components are parametrized by simple exponentials of the form $S_i(t) = A_i \exp(-\lambda_i t)$. All data is fit with the `musrfit` analysis framework [24].

Several single crystal specimens sourced from SurfaceNet (Rheine, Germany) were used: a $10 \times 10 \text{ mm}^2$ single crystal (C1) with the c -axis in plane and $[11\bar{2}0]$ out of plane, and $8 \times 8 \text{ mm}^2$ (C2) and $5 \times 5 \text{ mm}^2$ (C3) single crystals with the c -axis out of plane. The ZF data were taken on C1 with the c -axis oriented along \hat{x} to coincide with the initial spin direction. Small external fields were applied to C1 ($\mathbf{B}_{ext} \parallel [11\bar{2}0]$) and C2 ($\mathbf{B}_{ext} \parallel c$). High field experiments were carried out on C3 ($\mathbf{B}_{ext} \parallel c$).

III. RESULTS

The primitive unit cell of Cr_2O_3 is rhombohedral and contains 4 Cr atoms and 6 O atoms, see inset 1 in Fig. 1 (c). The Cr are arranged in two pairs along the rhombohedral 111-axis (c -axis), with the oxygens forming two triangles, rotated 60° with respect to each other, between

the Cr pairs. In the absence of magnetic order, the primitive unit cell is inversion symmetric, and there is three-fold rotation symmetry around the c -axis.

In oxides, muons are generally found to stop $\approx 1 \text{ \AA}$ away from an oxygen, similar to the hydrogen in a hydroxyl OH bond [25, 26]. Assuming this holds for Cr_2O_3 , we can use symmetry arguments to make some general statements about potential muon stopping sites. All six oxygens are crystallographically equivalent, thus any given muon sites close to one oxygen can be projected by either inversion or 120° rotations about c into another equivalent site. Consequently, there are at least six (or integer multiples thereof) electrostatically equivalent stopping sites within the primitive unit cell, which, when projected onto the c -plane through the inversion center, form a hexagon, see inset 2 in Fig. 1(c) and Fig. 8.

Due to localized electrons in the Cr $3d$ shell, there is a magnetic moment associated with each Cr. Below the Néel temperature $T_N = 307 \text{ K}$, those moments align pairwise opposite to each other along the c -axis, see inset 1 in Fig. 1(c), causing an internal magnetic field \mathbf{B}_{int} at the muon stopping sites. The magnetic structure breaks the inversion symmetry, $\mathbf{B}_{int}(\mathbf{r}) = -\mathbf{B}_{int}(-\mathbf{r})$. As a consequence, the *direction* of the internal fields associated with the various electrostatically equivalent sites is different. However, as the Cr moments are parallel to the c , the *magnitude* $|\mathbf{B}_{int}|$ at each of the sites is the same. Since only the magnitude determines the precession frequency, muons that stop in any one of the equivalent sites in zero external field precess with the same frequency and contribute to the same signal $S_i(t)$. From now on, we refer to an ensemble of electrostatically equivalent sites that have the same $|\mathbf{B}_{int}|$ as a *muon environment*. Note that at a given temperature, muons may stop in *different* environments with distinct $|\mathbf{B}_{int}|$.

We start with a presentation of the zero-field (ZF) results. Then, the effects of external magnetic fields \mathbf{B}_{ext} are described, first for fields small compared to the internal field ($\mathbf{B}_{ext} \ll \mathbf{B}_{int}$), then for large fields ($\mathbf{B}_{ext} > \mathbf{B}_{int}$).

A. Zero external field

A ZF μSR spectrum showing the muon spin polarization as a function of time and its Fourier transform (FT) taken at $T = 2.2 \text{ K}$ are displayed in Figs. 1(a) and (b). Three ZF precession frequencies f^{ZF} are observed, indicating three distinct muon environments, termed E1-E3. With increasing temperature, certain frequencies disappear, see Fig. 1(c). The frequencies are assigned to the environments E1-E3 in order of appearance: the frequency observed up to T_N is called f_{E1}^{ZF} , whereas f_{E2}^{ZF} can only be seen up to $\approx 190 \text{ K}$ and f_{E3}^{ZF} up to $\approx 60 \text{ K}$. All three precession frequencies increase with decreasing temperature, approximately tracking the sublattice magnetization.

The spectra contain both oscillating and non-

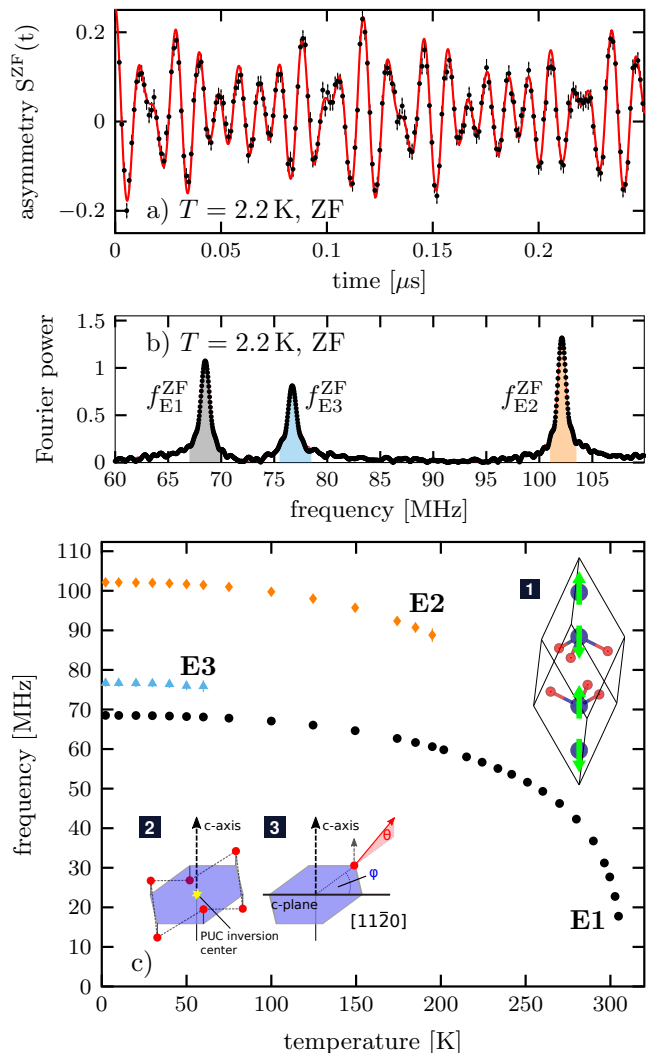


FIG. 1. (a) ZF μSR time-domain spectrum at $T = 2.2 \text{ K}$ and (b) its Fourier transform. (c) Observed ZF precession frequencies assigned to three muon environments, E1-E3, as a function of temperature. Insets: (1) Primitive unit cell of Cr_2O_3 with 4 Cr atoms (blue) along the c -axis, and 6 oxygen atoms. Below $T_N = 307 \text{ K}$, the Cr magnetic moments (green) align pairwise opposite along the c -axis. (2) Electrostatically equivalent stopping sites (red) form a hexagon when projected onto the c -plane through the inversion center. (3) Definition of angles describing the direction of the internal field at a given site.

oscillating components, and are fit with up to three damped cosines, Eqn. (1), a non-relaxing component and a relaxing component (nonzero only above $\approx 160 \text{ K}$).

The fit results for the oscillatory components associated with E1-E3 are shown in Fig. 2. The amplitude A_{E1} is constant up to 200 K , above which it increases and approximately doubles at T_N . Both A_{E2} and A_{E3} are approximately constant. The relaxation rates λ_{E2} and λ_{E3} increase sharply when approaching the temperature where their associated ZF frequency vanishes. While

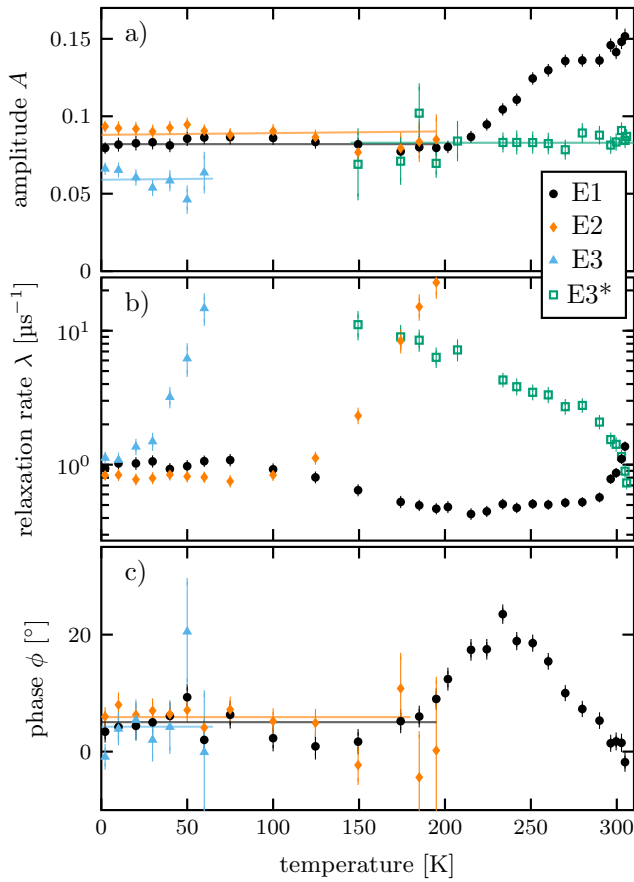


FIG. 2. Fit results for the three ZF oscillatory signals E1-E3 as a function of temperature: (a) amplitudes A (b) relaxation rates λ (logarithmic y-axis) (c) phase ϕ . Note the pronounced peak at around 240 K in the E1 phase, indicating a transition process between muon environments. Lines are guides to the eye. Additionally, the amplitude and relaxation rate for E3* are shown, see Section III B 2.

both phases ϕ_{E2} and ϕ_{E3} , shown in Fig. 2(c), can be considered constant, there is a pronounced peak in ϕ_{E1} between 200 K and T_N . As discussed in Section IV B, such a change in phase is indicative of a transition from another (so far unspecified) environment into E1, a hypothesis supported by the increase of A_{E1} at the same temperature. Aside from the precession signals, there is a sizable non-oscillatory relaxing component that appears above ≈ 160 K (not shown). This is attributed to the E3* component discussed below in Section III B 2.

B. Weak external fields

There are two main effects caused by weak external magnetic fields ($\mathbf{B}_{ext} \ll \mathbf{B}_{int}$), (1) the degeneracy of $|\mathbf{B}_{int}|$ for electrostatically equivalent stopping sites within one environment is lifted, and (2) a component precessing in \mathbf{B}_{ext} rather than \mathbf{B}_{int} appears.

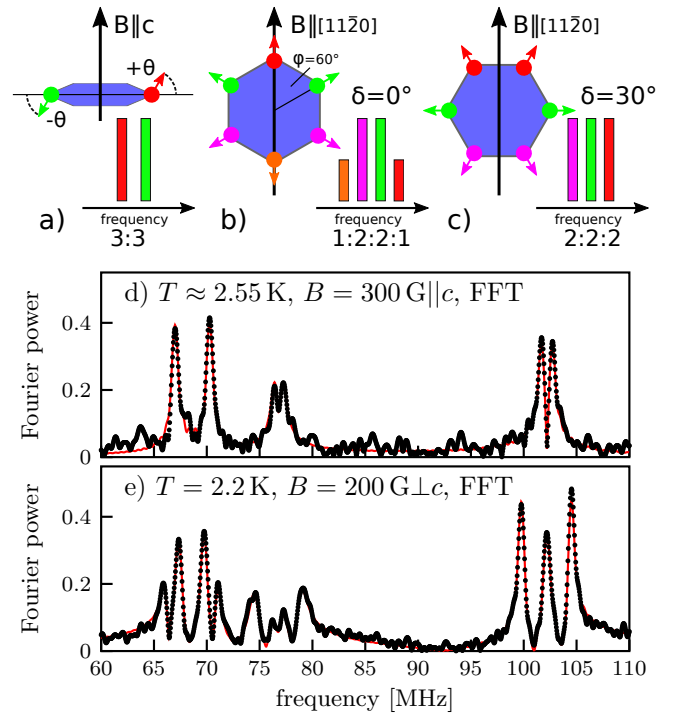


FIG. 3. Schematic illustration of how an external magnetic field breaks the degeneracy of $|\mathbf{B}_{int}|$ for stopping sites with the same magnitude, but different directions of \mathbf{B}_{int} . Only those sites shown in the same color share the same magnitude of the vector sum $|\mathbf{B}_{int} + \mathbf{B}_{ext}|$, resulting in a multiplet splitting and amplitude ratio as depicted: (a) $\mathbf{B}_{ext} \parallel c$ causes a doublet splitting, $\mathbf{B}_{ext} \perp c$ causes (b) a quadruplet ($\delta = 0$) and (c) a triplet splitting $\delta = \pm 30^\circ$; (d) FT of μ SR spectra in $B = 300$ G $\parallel c$ at $T = 2.55$ K and (e) FT of μ SR spectra in $B = 200$ G $\parallel [11\bar{2}0] \perp c$ at $T = 2.2$ K

1. Orientation of the internal magnetic field

The internal field direction at a stopping site can be described by two angles; θ is defined as the smallest angle enclosed by \mathbf{B}_{int} and the c -plane, and φ as the azimuthal angle (enclosed by $[11\bar{2}0]$ and the \mathbf{B}_{int} projection onto the c -plane), see insets in Fig. 1. From symmetry, stopping sites forming a given environment can be projected onto the c -plane to form a hexagon. The six φ values of an environment are given by $\delta + 0^\circ, \delta \pm 60^\circ, \delta \pm 120^\circ$ and $\delta + 180^\circ$, with δ being the smallest angle enclosed by $[11\bar{2}0]$ and a hexagon corner. As noted above, the internal field magnitude at the stopping sites forming a given environment is the same, but its direction is not. While this is inconsequential in ZF, the relative orientations of \mathbf{B}_{int} and \mathbf{B}_{ext} matter in the presence of external fields, where the precession frequency is determined by the magnitude of the vector sum $|\mathbf{B}_{int} + \mathbf{B}_{ext}|$. Consequently, the application of \mathbf{B}_{ext} lifts the degeneracy of the precession frequencies *within* an environment, causing multiplet splittings. This is schematically illustrated in Figs. 3 (a)-(c) both for $\mathbf{B}_{ext} \parallel c$ and $\mathbf{B}_{ext} \perp c$. The FTs of the μ SR

TABLE I. ZF precession frequencies f^{ZF} , θ and δ values describing the internal field orientation for E1-E3 at $T = 2.2$ K.

site	f^{ZF} [MHz]	θ [°]	δ [°]
E1	68.52 ± 0.01	24 ± 1	0 ± 3.5
E2	102.12 ± 0.01	6 ± 1	30 ± 3.5
E3	76.69 ± 0.01	5 ± 1	17.5 ± 2

spectra at low temperatures are shown in Fig. 3 for (d) $\mathbf{B}_{\text{ext}} = 300 \text{ G} \parallel c$ [27] and (e) $\mathbf{B}_{\text{ext}} = 200 \text{ G} \parallel [11\bar{2}0] \perp c$. Comparison with the ZF spectrum, Fig. 1(b), shows that for $\mathbf{B}_{\text{ext}} \parallel c$, the E1-E3 lines split into doublets, while for $\mathbf{B}_{\text{ext}} \perp c$, more complex multiplets are observed. The spectra were fit with up to 12 oscillatory signals, Eqn. (1), and a small non-oscillating signal. The obtained frequencies (f_{exp}) are shown in Table III and IV. Under the assumption that \mathbf{B}_{ext} does not induce changes of \mathbf{B}_{int} , all multiplet frequencies can be consistently described by the vector sum $|\mathbf{B}_{\text{int}} + \mathbf{B}_{\text{ext}}|$, which allows extraction of the θ and δ values describing the orientation of \mathbf{B}_{int} in E1-E3, see Table I for a summary and Appendix A for details. The obtained angles provide stringent criteria for comparison with the internal field of candidate muon sites calculated with DFT, see Section V.

2. Evidence for a signal component with zero internal field

Having discussed the effect of \mathbf{B}_{ext} on the precession frequencies, we now turn our attention to the non-precessing component that appears in ZF above ≈ 160 K. At coinciding temperatures and in both $\mathbf{B}_{\text{ext}} \perp c$ and $\mathbf{B}_{\text{ext}} \parallel c$ (not shown), there is a component of comparable amplitude that oscillates at the Larmor frequency of the external field ($f_{\text{ext}} = \gamma_{\mu}/2\pi|\mathbf{B}_{\text{ext}}|$), which is absent below 150 K, see Fig. 4. Spin precession about \mathbf{B}_{ext} rather than \mathbf{B}_{int} , in spite of ordered Cr moments, indicates that the muons giving rise to this signal are not subject to an internal field. The temperature dependence of the amplitude and relaxation rate of this signal, termed E3* in anticipation of its interpretation in Section IV B, is shown in Fig. 2.

C. Large external fields

The ZF spectra indicate that the highest \mathbf{B}_{int} is about 0.75 T. Here, we apply external fields significantly higher than this. The temperature dependence of the FTs of μSR spectra taken in $\mathbf{B}_{\text{ext}} = 4 \text{ T} \parallel c$ is shown in Fig. 5. Again, a doublet splitting is expected for each ZF frequency; however, since the position of f^{\pm} with respect to f^{ZF} depends on the relative strength of \mathbf{B}_{ext} to \mathbf{B}_{int} , and $\mathbf{B}_{\text{ext}} > \mathbf{B}_{\text{int}}$, f^{-} and f^{+} are distributed around f_{ext} rather than f^{ZF} , compare Figs. 3(d) with 5(a). At $T = 2.1$ K, five lines are observed. They can be

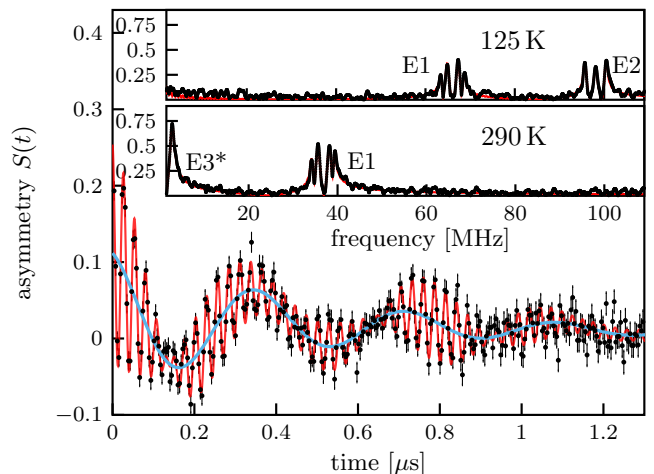


FIG. 4. μSR spectrum taken in $\mathbf{B}_{\text{ext}} = 200 \text{ G} \perp c$ at $T = 290$ K. Alongside the expected multiplet splittings, compare Fig. 3 (e), there is an additional component termed E3* that precesses at the (much lower) Larmor frequency of the applied field (blue line), indicating that some muons do not experience any internal field. Insets: FT at $T = 125$ K (top) and $T = 290$ K (bottom). The E3* line corresponding to precession in \mathbf{B}_{ext} is absent at lower temperatures.

assigned as follows: the two outer frequencies (colored in black) compose the E1 doublet f_{E1}^{\pm} , while the second (orange) and third (blue) highest frequencies correspond to f_{E2}^{+} and f_{E3}^{+} , respectively. The remaining line (uncolored) is a superposition of both f_{E2}^{-} and f_{E3}^{-} , explaining its large amplitude. The temperature evolution follows mostly what is expected from the ZF results. With increasing temperature, the E1 doublet splitting decreases as $|\mathbf{B}_{\text{int}}|$ decreases. Above 200 K, its amplitude becomes larger, and the line broadens approaching T_N . Likewise, f_{E2}^{+} follows the decreasing \mathbf{B}_{int} , and disappears above ≈ 185 K. For all temperatures where f_{E2}^{+} is observed, the uncolored line has a contribution from f_{E2}^{-} . Above ≈ 170 K, a large component close to f_{ext} appears, and is, in accordance with Section III B 2, assigned to E3*. The E3 doublet is only observable below 50 K.

Remarkably, there is an additional component between 50 K and 170 K, termed E3' (green in Fig. 5). As will be discussed in Section IV B, this additional line is strongly indicative of local hopping between adjacent E3 sites.

Details on the data analysis as well as fit results for the amplitudes can be found in Appendix B. From the multiplet splitting, θ values matching closely those obtained in low field are extracted, see Table V. This indicates that even in large \mathbf{B}_{ext} , \mathbf{B}_{int} is not significantly affected (reasonable since the Cr Zeeman energy in 4 T is much smaller than the exchange coupling [28]), and the precession frequencies are well determined by vector addition. The fitted frequencies are shown in Fig. 6. The red lines represent calculated doublet frequencies $f_{\text{E1}}^{\pm}(T)$ and $f_{\text{E2}}^{\pm}(T)$ assuming constant θ , see Appendix B for details. There is good overall agreement with the data, indicating

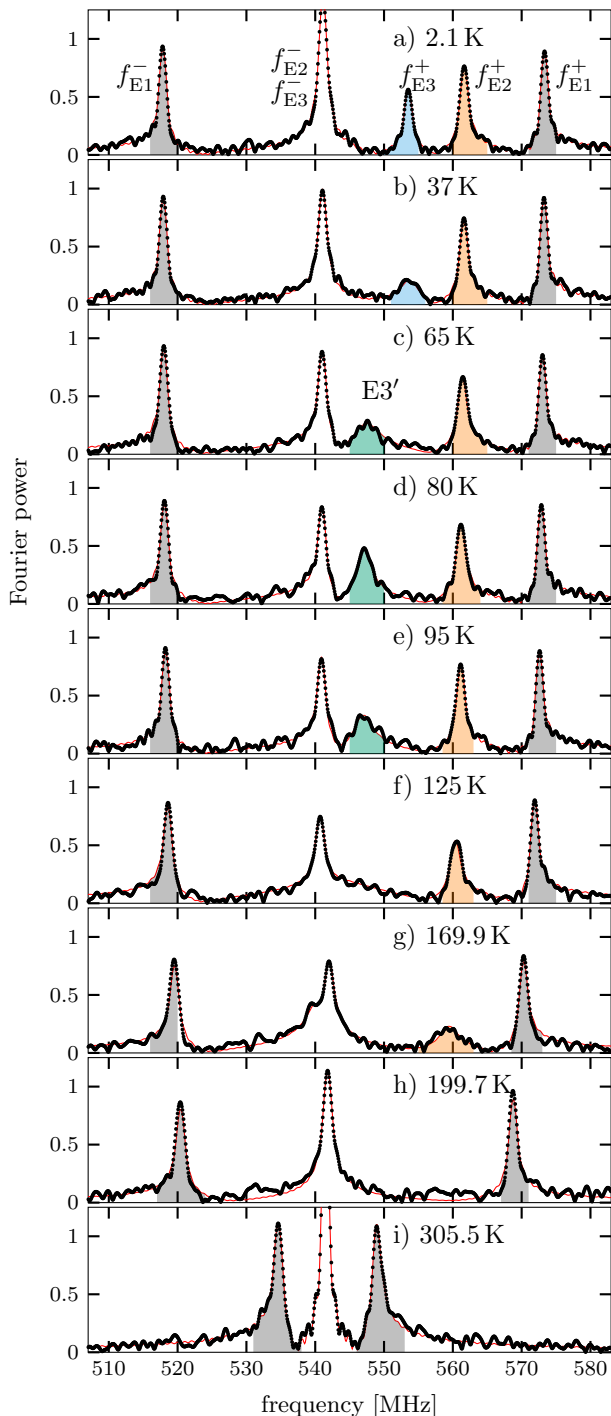


FIG. 5. Temperature dependence of FTs of μ SR spectra taken in $\mathbf{B}_{ext} = 4 \text{ T} \parallel c$.

that θ is largely temperature independent.

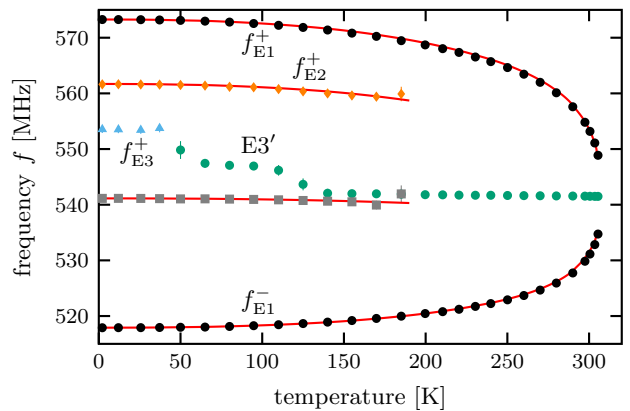


FIG. 6. Temperature dependence of frequencies obtained in $\mathbf{B}_{ext} = 4 \text{ T} \parallel c$. Solid lines are calculated doublet frequencies $f_{E1}^{\pm}(T)$ and $f_{E2}^{\pm}(T)$ assuming constant θ .

IV. EXPERIMENTAL EVIDENCE FOR SITE METASTABILITY AND DYNAMICS

Three ZF frequencies are observed, see Fig. 1(c), and attributed to three distinct muon environments, E1-E3. Each environment contains a number of electrostatically equivalent sites with the same magnitude, but different directions, of \mathbf{B}_{int} . Above $\approx 160 \text{ K}$, a component E3* precessing in the *external* rather than the internal field is observed both in low and high field, indicating an environment characterized by zero internal field.

The E2 and E3 signals disappear at different temperatures, while E1 is observed over the complete temperature range, indicating that each environment has a distinct potential energy. At low temperatures, E1-E3 are all populated. Since site populations are determined by the epithermal implantation process rather than thermodynamic equilibrium, it is possible that a muon occupies metastable sites with higher energy than the ground state. If thermally activated transitions to a lower energy state are inaccessible within its short lifetime, the muon may remain in the metastable site and give rise to a distinct signal [29, 30]. However, with increasing temperature, site changes either within one, or into another environment may become possible.

Around 180 K, E1, E2 and E3* signals are observed and account for the full signal, see Fig. 2(a). Noting that the amplitudes of both E2 and E3* are approximately temperature independent in the respective regions where they are observed, we conclude that (1) muons in E2 do not transition into E3*, (2) thus the disappearance of E2 stems from a transition into E1 at sufficiently high temperatures and (3) consequently, by conservation of total amplitude, muons that stop in E3 below 50 K must give rise to E3* at higher temperatures.

In this section, we first present a model supporting the E2 \rightarrow E1 transition. Then, the evolution of muons from E3 into E3* is discussed in terms of local muon hopping between adjacent, electrostatically equivalent E3 sites.

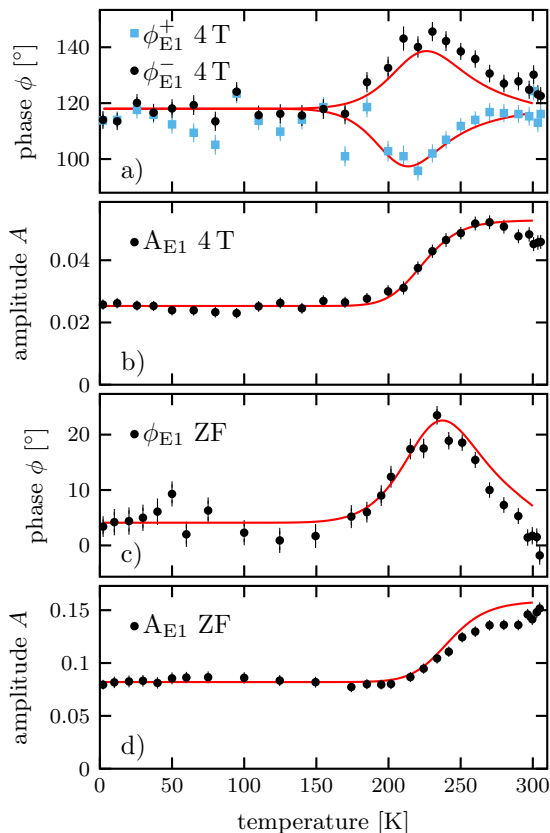


FIG. 7. Comparison of experimental E1 phase and amplitude with the E2→E1 transition model for (a) ϕ_{E1} in 4 T, for f_{E1}^+ (blue) and f_{E1}^- (black) (b) E1 amplitude, as obtained by a shared fit of the f_{E1}^\pm doublet. (c) ZF ϕ_{E1} and (d) ZF amplitude. Solid lines are Eqns. (C2) and (C3) with shared model parameters $E_a = 180$ meV and $\nu_0 = 8 \times 10^{11}$ Hz.

A. E2 - E1 transition

Here, we show that the disappearance of the E2 signal around 200 K, and the subsequent increase in E1 amplitude is consistent with a metastable E2 environment that allows for transitions into E1. The following discussion is based on two assumptions: (1) The E2→E1 transition can be described by a thermally activated, exponential rate of the form $\Lambda(T) = \nu_0 \exp(-E_a/k_B T)$, where E_a and ν_0 are the activation energy and attempt frequency. (2) At the time of implantation, the probability for the muon to initially occupy a site in any of the three environments is temperature independent (i.e. at all temperatures, the same fraction of muons start out in E1, E2 and E3). This assumption is discussed in Sec. VI. While the initial fraction starting in E2 is independent of temperature, the actual time spent in this environment depends on the transition rate $\Lambda(T)$. If $\Lambda(T)$ is much smaller than f_{E2} , the E2 muons precess for many periods with f_{E2} before transitioning, and oscillatory signals from both E1 and E2 with amplitudes A_{E1} and A_{E2} can be detected. In contrast, if $\Lambda(T)$ is much larger than f_{E2} ,

the E2 muons change to E1 before the muon spin has a chance to precess with f_{E2} , and a single oscillatory signal at f_{E1} with a combined amplitude $\mathcal{A} = A_{E1} + A_{E2}$ can be observed. However, if $\Lambda(T)$ is comparable to f_{E2} , the E2 muons may precess at f_{E2} prior to the transition, and acquire a phase shift with respect to muons initially in E1. This results in a smaller apparent E1 amplitude \mathcal{A} and an overall phase shift $\Phi(T)$. In Appendix C, a model accounting for such a transition and expressions for $\mathcal{A}(T)$ and $\Phi(T)$ are described. In Fig. 7, the E1 phase and amplitude data of both the ZF signal and the high-field doublet are compared with the transition model, with activation energy $E_a = 180$ meV and attempt frequency $\nu_0 = 8 \times 10^{11}$ Hz being *shared* parameters for the *complete* data set.

There is excellent qualitative agreement between the model and the data; the peak in the phase, including the opposite direction for the high field doublet, and the increase in amplitude are well described both in ZF and high field with the same parameter set. Thus the proposed E2→E1 transition with an estimated barrier $E_a = 180 \pm 40$ meV provides a consistent explanation for the disappearance of the E2 signal, its associated increase in relaxation rate, and the subsequent increase in E1 signal amplitude.

B. Local hopping

Next, we show that both the E3 frequency observed below 50 K and the E3* signal precessing at the Larmor frequency of the external field arise from muons in the *same* environment. The appearance of E3* above ≈ 160 K, see Figs. 4 and 5, indicates that a fraction of muons experience no internal field. This is surprising since the simultaneous observation of the E1 signal clearly shows the presence of ordered Cr magnetic mo-

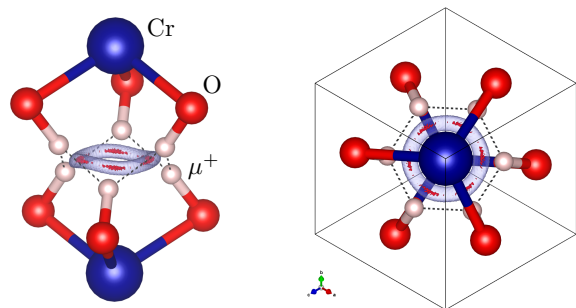


FIG. 8. Example configuration of electrostatically equivalent muon sites, based solely on symmetry considerations and the constraint that muon stopping sites (white spheres) are located 1 Å away from oxygen (red spheres). The close proximity of nearby sites suggests localized hopping. The electrostatic potential isosurface of the *undistorted* crystal structure is shown in blue, with the red patches indicating local electrostatic minima, corresponding to the position of the so called Rodriguez (R) sites [31].

ments. Although there are high-symmetry sites along the c -axis where the internal field precisely cancels, these sites are far ($\gg 1 \text{ \AA}$) from an oxygen and energetically unfavorable for an interstitial μ^+ site, as confirmed by DFT in Section V. Instead, we consider in Fig. 8 an example configuration of one environment comprised of six electrostatically equivalent muon stopping sites (white spheres), based solely on symmetry considerations (see beginning of Section III), and a muon-oxygen distance of 1 \AA . Given the close proximity of nearby electrostatically equivalent sites, thermally activated local hopping between adjacent sites seems plausible. For sufficiently fast intra-environment hopping, the effective internal field experienced by the dynamic muon is the average over all sites. Noting $\mathbf{B}_{int}(\mathbf{r}) = -\mathbf{B}_{int}(-\mathbf{r})$ and the symmetry of equivalent sites, it becomes clear that this average is *zero*. We hypothesize that muons stopping in E3 sites undergo such local hopping around a single hexagon at elevated temperatures, leading to the disappearance of the f_{E3}^{ZF} signal, and the subsequent observation of the E3* signal in an external field.

This consistently explains the observed data: at low temperatures, muons stopping in E3 sites are quasi-static, i.e. no or only very slow hopping occurs, and each muon precesses predominately in the internal field of *one* site, giving rise to f_{E3}^{ZF} . Above $\approx 160 \text{ K}$, a relaxing non-oscillatory component appears in ZF, consistent with a fraction of muons that are not subject to any field. In the intermediate temperature region $60 - 160 \text{ K}$, no signal is observed, as the hopping is neither fast enough to efficiently average out the internal field, nor slow enough to allow for the observation of coherent E3 oscillations. External fields, both small and large, cause multiplet splittings of f_{E3} at low temperature, consistent with muons being quasi-static, while above $\approx 160 \text{ K}$, a signal precessing in \mathbf{B}_{ext} can be observed (E3*), since \mathbf{B}_{int} is averaged to zero and does not contribute to the field magnitude. In high field, an additional signal, E3', see Fig. 5, is observed in the intermediate temperature region. A Monte Carlo simulation of the muon depolarization function in $4 \text{ T} \parallel c$, assuming local hopping, identifies E3' as the average of the doublet frequencies $f_{E3}^{avg} = (f_{E3}^+ + f_{E3}^-)/2$, and allows for an estimate of the energy barrier between E3 sites $E_b = 42 \pm 5 \text{ meV}$, see Appendix D for details on the simulation and an in-depth discussion. Overall, we clearly show that the E3/E3'/E3* signals arise from different dynamic regimes of muons undergoing local hopping in a *single* environment.

Already in the first μSR paper on antiferromagnets, local diffusion between electrostatically equivalent sites was considered a possibility in Fe_2O_3 [31]. Subsequently, local motion was speculated to occur in Cr_2O_3 [23], and is suspected [25, 32] and observed [33–35] in a range of materials. Here, we conclusively show that local hopping indeed occurs in Cr_2O_3 by direct observation, identification and consistent description of the distinct signals that arise as a result of restricted motion in a system with broken magnetic inversion symmetry, a hop rate

changing several orders of magnitude over the observed temperature range, and various applied fields.

We further note that muons in both E1 and E2 are, apart from the E2→E1 transition, site-stable, i.e. no intra-environment motion occurs. This is evident from the pronounced multiplet splitting that is observed at all temperatures where E1 and E2 signals are detected, see Figs. 4 and 5.

V. IDENTIFICATION OF MUON STOPPING SITES WITH DFT

Thus far, using simple models describing a thermally activated E2→E1 transition and local hopping within the E3 environment, and without explicit knowledge of the stopping sites, we have explained the major features in the data. The coexistence of site-stable and highly mobile muons is intriguing, especially since there is no evidence for interexchange between dynamic E3 muons and static E1 or E2 muons, even in the presence of the E2→E1 transition. To gain deeper insight into this surprising behavior, we turn to DFT to identify muon stopping sites. With the recent increase in availability and capability of computing resources countering the large computational demands of first principles calculations, DFT has had great success in providing information about location and stability of muon stopping sites in a range of materials, and is developing into an important new tool for μSR (see Ref. 36 for a review, and Refs. 37 and 38 for recent developments).

Since the inception of the μSR technique, knowledge of the location of the muon within the sample was of key importance. The main motivation for the early μSR studies on antiferromagnets, prompted by the first observation of ZF μSR signals in Fe_2O_3 [31] and its isomorph Cr_2O_3 [20], was to establish the muon as a sensitive and useful probe of the local magnetic properties of the host material by determining (1) where the muon stops and what its dynamic properties are with respect to site stability and diffusion and (2) if, and under what conditions muonium is formed in insulating (anti)ferromagnets. Based on simple electrostatic considerations, two sets of possible stopping sites were found for the Corundum structure, so called Rodriguez (R) sites [31] located in the Cr gap close to the inversion center, see Fig. 8, and Bates (B) sites [22] in (B0), or slightly above and below (B1) the oxygen basal plane, see Fig. 2 in Ref. 23. The internal magnetic field in these sites was estimated by summing over the dipolar contributions from surrounding Cr moments. Additionally, covalency effects were considered, and attempts to assign ZF frequencies to specific sites yielded some partial and approximate agreements, although the overall results remained inconclusive [22, 23]. No evidence for Mu or a neutral charge state was identified.

We have calculated the muon stopping sites in Cr_2O_3 using the Vienna ab initio Simulation Package [39–41], see Appendix E for details. The positive muon was mod-

CS	E	Site	d_{z^2}	f_{dip} [MHz]	f_c [MHz]	f_{tot} [MHz]	θ [°]	φ [°]	ΔE [meV]
+	E3	D		94.1 ± 0.0	2.8 ± 4.4	93.9 ± 0.4	3.8 ± 2.9	4.5 ± 0.0	0
		B0		28.2 ± 2.2	0.0 ± 0.0	28.2 ± 2.2	0.1 ± 0.0	29.5 ± 0.0	753
		C_O		99.1 ± 4.0	49.4 ± 14.0	55.9 ± 10.0	90.0 ± 0.0	1.3 ± 1.2	1565
		C_E		0.0 ± 0.0	0.0 ± 0.0	0.0 ± 0.0	90.0 ± 0.0	57.4 ± 0.0	1728
0	E1	D1	\uparrow	72.4 ± 0.3	35.6 ± 3.3	78.0 ± 1.0	-22.4 ± 2.5	35.8 ± 0.5	0
	E2	D2	\downarrow	114.4 ± 0.2	3.9 ± 18.4	114.3 ± 1.4	0.0 ± 8.9	58.9 ± 0.7	116
		D3	\downarrow	119.0 ± 0.8	1.6 ± 17.4	118.6 ± 6.8	-17.3 ± 7.8	5.5 ± 0.1	320
		D4	\uparrow	100.9 ± 0.3	3.8 ± 3.2	100.4 ± 0.6	5.9 ± 2.1	58.3 ± 0.3	419
		D5	\uparrow	82.9 ± 0.4	34.7 ± 4.1	99.3 ± 2.2	-37.4 ± 2.5	39.7 ± 0.3	448
		B1		92.1 ± 0.2	430 ± 30	470 ± 30	-79.4 ± 0.7	24.0 ± 0.1	945
		B0		47.4 ± 1.8	0.2 ± 0.1	47.3 ± 1.8	-17.7 ± 0.8	30.3 ± 0.0	1157
		C_O		94.3 ± 1.2	581.3 ± 26.7	486.7 ± 25.5	-90.0 ± 0.0	-	355
		C_E		0.0 ± 0.0	0.0 ± 0.0	0.0 ± 0.0	90.0 ± 0.0	-	1206

TABLE II. DFT results for various candidate sites and two charge states (CS): dipolar f_{dip} and contact contributions f_c giving rise to the combined f_{tot} , which spans the angles θ and φ as defined in III B 1. ΔE is the energy relative to the ground state of each charge state respectively, and d_{z^2} the spin state of the extra electron for D1⁰-D5⁰. Shaded rows indicate candidates for E1-E3.

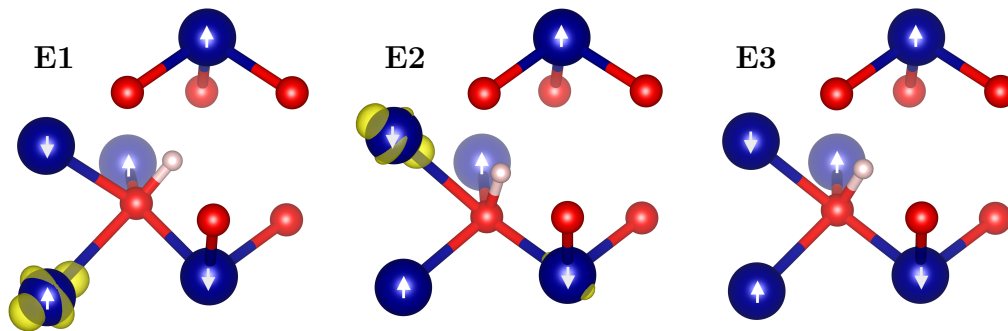


FIG. 9. Candidate muon stopping sites for E1-E3 (white spheres) identified using DFT. Transparency indicates a location *behind* the solid atoms. Yellow iso-surfaces indicate the spin density of the top-most occupied level (d_{z^2}) for the charge neutral E1 and E2 sites. Arrows indicate direction of magnetic moment.

eled as a hydrogen nucleus, embedded within an 80-atom $2 \times 2 \times 2$ rhombohedral supercell (SC) of Cr_2O_3 . Two muon charge states were considered (1) the bare, positive muon, with a uniform charge background ensuring overall charge neutrality and (2) a neutral muon state allowing for the extra electron. As a first step, promising initial muon positions were identified. Given the muon's tendency to form a muon-O bond of length $\sim 1 \text{ \AA}$, a set of 99 initial configurations were generated with the muon positions equidistributed on a 1 \AA sphere centered on an oxygen. Since all oxygen atoms are electrostatically equivalent, it is sufficient to perform this search on a single oxygen. Initial static calculations of the Hellmann-Feynman forces allowed us to discard sites with forces larger than 10 eV/\AA . For the remaining sites, the Cr_2O_3 ions were relaxed while keeping the muon fixed. This initial step of relaxing only the lattice allowed for a search for self-trapped metastable sites. Finally, both the muon and lattice were fully relaxed until the Hellmann-Feynman forces were below 5 meV/\AA . Additionally, muons were started out in the R and B sites, and in the unit-cell center - both the exact center (C_E) and slightly offset along the c -axis (C_O). The structure files of all candidate stopping sites for both charge states are available in the Supplemental Information [42].

The total hyperfine field \mathbf{B}_{tot} at each site \mathbf{r}_μ has (1) a dipolar contribution \mathbf{B}_{dip} mainly from the Cr $3d$ electrons, and (2) a Fermi contact term \mathbf{B}_c from unpaired spin density $\rho_s(\mathbf{r}_\mu)$ at the muon stopping site. \mathbf{B}_{dip} was calculated by embedding the distorted $2 \times 2 \times 2$ SC in a

superstructure of undistorted SCs and summing over the dipolar contribution from the spin density grid points. Despite a fine grid spacing of 0.055 \AA , the finite grid causes artifacts for points in close proximity to \mathbf{r}_μ . This is mitigated by excluding grid points less than $R = 0.5 \text{ \AA}$ away from \mathbf{r}_μ . \mathbf{B}_c is calculated by [37]

$$\mathbf{B}_c = \frac{2}{3} \mu_0 \mu_B \rho_s(\mathbf{r}_\mu) \hat{c}, \quad (2)$$

where μ_0 is the vacuum permeability and μ_B the Bohr magneton. $\rho_s(\mathbf{r}_\mu)$ is approximated by projecting the spin density within a $R = 0.5 \text{ \AA}$ sphere onto an s-wave state at the μ^+ .

Results for both charge states (positive and neutral) are shown in Table II. Calculated fields are given in units of frequency $f_i = \frac{\gamma_\mu}{2\pi} |\mathbf{B}_i|$. Note that f_{tot} is obtained by *vector* addition $|\mathbf{B}_{dip} + \mathbf{B}_c \hat{c}|$. The energies ΔE are given with respect to the ground state and are only comparable within a given charge state. The stated uncertainties are estimated by varying the sphere radius R for both the contact and dipole term calculations in the range $0.3 - 0.7 \text{ \AA}$.

For the positive charge state (superscripted +), the B1⁺ site cannot be stabilized, and muons placed in the primitive unit-cell center (C sites) can be discounted as viable muon stopping sites based on magnitude and direction of \mathbf{B}_{int} , and large ΔE . For the same reasons, B0⁺ is unlikely to represent a muon stopping site. Unless purposefully placed in a B⁺ or C⁺ site, muons relax into a position close to but distinct from the R-sites (the electrostatic minima of the undistorted lattice). We name

this site D due to the doughnut-shaped potential energy surface formed by electrostatically equivalent sites. The difference between D and R arises predominantly from the muon-induced lattice distortion, which was not accounted for previously. The close proximity of adjacent D^+ -sites makes them excellent candidates for the E3 environment. Possible explanations for the discrepancy of 22% between $f_{E3}^{ZF} = 76.7$ MHz and the calculated value are discussed below.

While DFT calculations considering the positive muon can account for E3 muons undergoing local hopping, E1 and E2 are thus far unexplained, motivating a search for charge-neutral muon states. Results are shown in the bottom half of Table II. $B0^0$, $B1^0$ and C_E^0 can be dismissed based on large ΔE , and C_O^0 based on the large f_{tot} . This leaves five variations of the D^0 site, labeled $D1^0$ - $D5^0$. Comparison with Table IV and consideration of the calculated energies suggest that $D1^0$ and $D2^0$ are candidates for E1 and E2, respectively: the measured and calculated frequencies of for E1 (+14%) and E2 (+12%) and θ agree reasonably well and $\Delta\varphi(E2-E1)$ is close to the expected 30° , compare Table I. Additionally, consistent with the proposed $E2 \rightarrow E1$ transition, $D2^0$ has a larger energy than $D1^0$. The differences between $D1^0$ - $D5^0$, and further aspects of the $D2^0 \rightarrow D1^0$ transition are discussed below. Fig. 9 shows the positions of the E1-E3 candidate stopping sites $D1^0$, $D2^0$ and D^+ .

A more detailed analysis of the charge-neutral D^0 states reveals that the extra electron localizes predominantly on a nearby Cr, where it changes the valence from Cr^{3+} to Cr^{2+} , and singly occupies the initially orbitally degenerate e_g orbitals. This causes a Jahn-Teller distortion [7] by further elongating the Cr-O bond of the oxygen the muon is bound to from 2.18 Å for the bare muon to 2.43 Å in the charge neutral case, see Fig. 10. The subsequent lowering of energy, see Fig. 10, stabilizes this charge-neutral complex of a negatively charged JT polaron [8, 9] and positive muon. This proposed mechanism is supported by the extra electron occupying the lowered e_g level d_{z^2} , see yellow isosurface representing the charge density of top-most occupied band in Fig. 10. We note the similarity to the paramagnetic Ti-O-Mu complex recently observed in (nonmagnetic) TiO_2 [43, 44], where an unpaired electron sits on a nearby Ti atom, and the oxygen-bound muon forms a complex with the resulting small polaron. Crucially, however, the muon-polaron complex reported on here is not paramagnetic and therefore *distinct from Mu*, since the bound electron is strongly coupled to the 3d electrons of the Cr host ion. This is discussed in detail in Sec. VI.

The $D1^0$ - $D5^0$ states arise from the extra electron being localized on different Cr and small variations in the muon position. A transition between D^0 states is mainly characterized by a change in position of the extra electron rather than the muon. Note that the spin of the extra electron, being coupled to the 3d electrons of its Cr host, may be different for different D^0 states, as indicated in Table II. We propose that the higher energy states $D3^0$ -

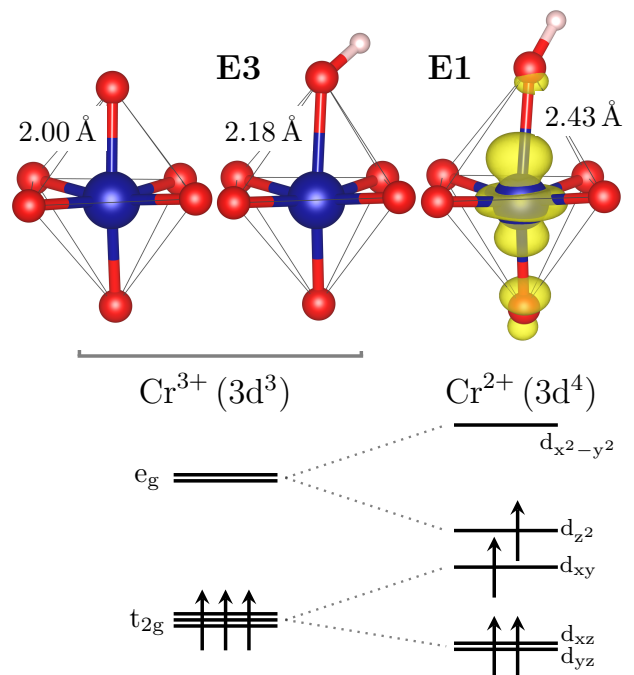


FIG. 10. Top: Octahedrally coordinated Cr atom (1) without the muon, with (2) the positive muon and (3) a neutral charge state formed by the muon and an extra electron localized on the Cr, changing its valence state from Cr^{3+} to Cr^{2+} . The presence of the positive muon removes some electron density from its associated Cr-O bond, causing elongation from 2.00 Å to 2.18 Å. The localization of the extra electron arising from the Coulomb attraction of the muon and the energy gain from the lattice distortion further elongates the Cr-O bond to 2.43 Å and leads to the formation of a charge-neutral muon-polaron complex. Bottom: Schematic representation of the crystal field: the occupation of the degenerate e_g orbital by the extra electron leads to a Jahn-Teller distortion. The yellow isosurface shows the charge density of the top-most occupied band for the charge-neutral case, confirming that indeed the d_{z^2} level is occupied.

$D5^0$ are not occupied since they can easily transition into either $D1^0$ or $D2^0$ depending on their spin. However, going from $D2^0$ into the ground state $D1^0$ requires an electron spin flip, i.e. an additional energy barrier has to be overcome. While the precise process for the $E2 \rightarrow E1$ transition is still under investigation, we attribute the observation of the metastable E2 environment to the existence of such a spin barrier.

In general, the energy barrier to move the joint muon-polaron complex is expected to be significantly larger than for the bare muon [45], providing a compelling explanation for the stability of E1 and E2, and coexistence of site-stable muons and highly mobile muons in E3.

Note that DFT local field predictions depend on the approximation of the exchange-correlation functional and value of the U_{eff} parameter. By comparing the LDA, PBEsol and SCAN functionals with a reasonable range

of U_{eff} corrections, we find variations in the predicted frequency magnitudes of $\sim 15\%$, in the θ angle of $\sim 60\%$ and in the ϕ angle of $\sim 10\%$ with respect to the LDA+ $U_{\text{eff}} = 4$ eV values, see Supplemental Information [27].

Finally, we note that an accurate consideration of the zero-point motion of the muon is necessary to calculate the formation energies of the different charge states [46], and the energy barriers for intra-E3 hopping and the E2→E1 transition. While a full treatment of the quantum nature of the muon is beyond the scope of the present paper, work is currently ongoing and will be published separately.

VI. DISCUSSION

Paramagnetic Mu centers are expected to be subject to fast relaxation in magnetic materials [3]. In the previous sections, we presented strong evidence for the formation of a charge-neutral muon-polaron complex in Cr_2O_3 , that, while not exhibiting signatures conventionally expected from neutral charge states, significantly influences the muon behavior and contributes a well-resolved signal. In particular, rather than giving rise to a well-defined spectrum of typically two or four precession frequencies that are determined by a spin Hamiltonian involving the muon and electron Zeeman energies and a muon-electron hyperfine interaction [1], the precession signal for the muon-polaron complex in Cr_2O_3 consists of a single frequency much like the normal positive charge state, i.e. the bare μ^+ with no additional electron nearby. The reason for the different behavior compared to that of Mu is that the muon-polaron complex is *not paramagnetic*, since its bound electron is strongly coupled to the $3d$ electrons of the Cr host ion, which themselves are antiferromagnetically coupled to the ordered network of magnetic ions of the host. We note that the bound electron is not centered on the μ^+ but localizes on a nearby Cr, which is not unique to the muon-polaron complex, since similar situations are found for the paramagnetic Mu complex in TiO_2 [4, 43, 44], and bond-centered Mu in silicon [47].

The relevance of the discovery of a muon-polaron complex in Cr_2O_3 may extend to other magnetic oxides, such as CuO [32, 48], Fe_2O_3 and FeTiO_3 [23], Fe_3O_4 [49] and the orthoferrites [26], which all show multiple zero-field precession frequencies that, while attributed to metastable sites, are not conclusively explained. In general, our study suggests that neutral charge states and their potential impact on crystal-field levels have to be carefully considered in all *insulating* magnetic materials, and that detailed DFT calculations can be used to separate intrinsic magnetic properties from muon-induced effects.

We emphasize that the present muon-polaron complex is different from the controversial concept of a muon-induced magnetic polaron proposed by Storchak *et al* [50–53], which invokes a localized electron bound

to a muon mediating a ferromagnetic coupling between neighboring magnetic ions, resulting in a “ferromagnetic droplet” characterized by a gigantic local spin.

We speculate that muon-polaron complex formation in Cr_2O_3 occurs by a similar mechanism to Mu formation in semiconductors [5]. Upon implantation, the muon slows down by creating electron-hole pairs. Towards the end of its ionization track it may capture an electron and subsequently form a charge-neutral complex. The implantation and electron capture processes are epithermal, and thus independent of sample temperature and thermodynamic equilibrium, providing justification for the previously stated hypothesis that E1-E3 are populated with the same ratio at all temperatures. Muons may stop and self-trap in metastable (charge) states with energies larger than the ground state, and only de-excite if thermally activated transitions, e.g. from E2 to E1, are accessible during the muon lifetime [29, 30].

Paramagnetic Mu has been used extensively to investigate the dopant characteristics of hydrogen in a wide range of semiconductors including oxides [2–5]. This is because the electronic structure of Mu in a solid is virtually identical to that of hydrogen, aside from small differences caused by the larger zero-point motion due to the lighter muon mass. We propose that with the observation of a neutral charge state in Cr_2O_3 , μSR has shown its ability to investigate the behavior of interstitial hydrogen in magnetic oxides as well. A thorough understanding of unintentional hydrogen doping in such materials is crucial, since a wide range of technologically relevant fields such as dilute magnetic semiconductors for spintronics [54–57] and superconductivity depend on a precise control of charge carriers in magnetic oxides, or, for example in the case of multiferroics, require low-leakage thin films [58].

Interestingly, interstitial hydrogen is predicted to form a shallow donor state in Cr_2O_3 , alongside a range of other materials including the aforementioned CuO, Fe_2O_3 and FeTiO_3 [59]. The observation of E1 up to T_N suggests that the muon-polaron complex stays intact up to room temperature, indicating that hydrogen is instead a deep impurity. This is in contrast to an ongoing study of muon-polaron complexes in Fe_2O_3 (to be published separately), which suggests complex ionization above 200 K, indicating shallow donor behavior. We note that Cr^{2+} with $3d^4$ high spin is strongly JT-active, while Fe^{2+} with $3d^6$ high spin is weakly JT-active, and hypothesize that donor characteristics are determined, at least in part, by the strength of the JT effect. The role of magnetic interactions in the stabilization of the muon-polaron complex remains an open question.

The prediction of hydrogen induced n -type conductivity in ZnO [46] and the subsequent experimental observation of the corresponding shallow Mu donor state [60] prompted a search for criteria to predict dopant behavior and charge state of interstitial hydrogen and muons, leading to generalized principles for elemental and binary semiconductors [57] and oxides [4, 59, 61, 62]. We hope

that our discovery of a JT-stabilized muon-polaron complex stimulates research to extend those principles to explicitly account for polaronic, and if required, magnetic contributions. Such adjusted criteria could provide valuable guidelines on whether or not neutral charge states are expected in μ SR experiments on insulating magnetic materials.

Lastly, having acquired a detailed understanding of how the muon interacts with Cr_2O_3 , we address possible implications arising from implanting a point charge into a linear magnetoelectric (ME) material. Khomskii predicts that a point charge inside an isotropic linear ME is surrounded by a monopole-like magnetic texture, and subject to a force in applied magnetic fields [19]. The monopolar magnetic field distribution is only expected sufficiently far from the charge where the bulk approximation holds, while no predictions are made for the immediate core region. The case of a muon inside Cr_2O_3 is more complex since (1) the ME coupling is not isotropic [13], (2) some muons are bound in a muon-polaron complex, an effectively charge-neutral entity, and (3) the muon induces significant lattice distortions in its immediate vicinity and experiences a magnetic field dominated by the core region which cannot be treated in the bulk limit. Thus the muon may sense a change in its magnetic environment in response to the electric field of its charge, arising from changes in the position of magnetic ions and canting of magnetic moments in its immediate environment, i.e. a *local* ME effect, however such an effect may not necessarily follow the bulk ME coupling. Results from preliminary non-collinear DFT calculations suggest only a small spin canting $< 0.3^\circ$ in the immediate neighborhood of the muon, however the elevated ME coupling at higher temperatures is not yet taken into account. We note that while the ME response outside the core region is expected to have monopolar contributions only in linear ME materials, muon-induced local ME effects may occur in non-ME compounds as well. Finally, we comment on the prediction that a static charge inside a ME is subject to a force in a magnetic field [19]. Using a lower limit of $1 \text{ eV}/\text{\AA}^2$ for the force constant of the potential experienced by the muon bound to an oxygen, the change in position in response to a field-induced force on the muon can be estimated to be smaller than 10^{-5} \AA in 4 T, i.e. is negligible in the context of this experiment. Despite the challenges discussed above, the investigation of local ME effects induced by the muon in its duality as a test charge and sensitive probe for magnetism remains a fascinating area of research, and we hope that the present paper initiates studies both experimental and theoretical in this direction.

VII. CONCLUSIONS

In summary, we carried out a comprehensive μ SR study of Cr_2O_3 under zero-field conditions and in applied magnetic fields. In zero field, we observe three

spin precession frequencies, attributed to three distinct muon environments E1-E3 with different internal magnetic fields. Small applied magnetic fields along various symmetry directions split the observed frequencies into multiplets, providing detailed information on the orientation of the internal fields. The temperature dependence reveals a rich dynamic behavior that we explain in terms of a thermally activated transition between E2 and E1, and intra-E3 local muon hopping. Notably, we observe coexistence of highly dynamic E3 muons and site-stable muons in E1 and E2. Muon stopping sites and charge states for all three environments are determined using DFT, and the coexistence is explained by the formation of a charge-neutral, JT-stabilized muon-polaron complex. The identification of such a charge-neutral complex in the antiferromagnet Cr_2O_3 has implications for other magnetic oxides, since the formation of muon-polaron complexes can significantly influence the stability and location of stopping sites, but its existence may be “hidden” since the behavior conventionally associated with neutral charge states is not displayed. Furthermore, this discovery opens up a route to study interstitial hydrogen in magnetic oxides, where precise control of the carrier density may be critical for device functionalities. Given the technological importance of magnetic oxides, we hope this study stimulates a search for generalized principles describing the dopant behavior of hydrogen that account for polaronic, and if required, magnetic contributions.

ACKNOWLEDGMENTS

This research was performed at the TRIUMF Centre for Materials and Molecular Science. The authors thank R. Abasalti and D. Vyas for excellent technical support. Initial spectra were taken at the Swiss Muon Source $S\mu S$ at PSI. We thank S. R. Dunsiger for critical reading of the manuscript and helpful discussions, and G. Levy for help with crystal alignment. MHD acknowledges support from a SBQMI QuEST Fellowship, and would like to thank A. Nojeh and I. Elfimov for stimulating discussions. Financial support came from a NSERC Discovery grant to RFK. JKS and NAS acknowledge funding from the European Research Council (ERC) under the European Union’s Horizon 2020 research and innovation programme grant agreement No 810451. Computational resources were provided by ETH Zürich and the Swiss National Supercomputing Centre, project ID s889. SH acknowledges financial support by the Swiss National Science Foundation (SNF-Grant No. 200021-159736). Crystal structures were drawn using VESTA [63].

Appendix A: Details on internal magnetic field orientation

Under the assumption that \mathbf{B}_{ext} does not induce changes of \mathbf{B}_{int} , the resulting frequency multiplets can

be calculated by simple vector addition. For $\mathbf{B}_{ext} \parallel c$, only θ is relevant, and we expect the ZF frequency f^{ZF} to be split into a doublet, see Fig. 3(a), with the frequencies f^\pm given by

$$f^\pm = \left[(f_{ext} \pm f^{ZF} \sin(\theta))^2 + (f^{ZF} \cos(\theta))^2 \right]^{1/2}, \quad (\text{A1})$$

where $f_{ext} = \gamma_\mu / (2\pi) \cdot |\mathbf{B}_{ext}|$. Given the equal number of sites with $+\theta$ and $-\theta$, equal amplitudes for both doublet lines are expected (for $\mathbf{B}_{ext} \ll \mathbf{B}_{int}$).

For $\mathbf{B}_{ext} \parallel [11\bar{2}0] \perp c$, the multiplet splitting, determined by both φ and θ , is given by

$$f(\theta, \varphi) = \left[(f^{ZF} \sin(\theta))^2 + (f^{ZF} \sin(\varphi) \cos(\theta))^2 + (f_{ext} + f^{ZF} \cos(\varphi) \cos(\theta))^2 \right]^{1/2} \quad (\text{A2})$$

Only for $\delta = 0$ or $\pm 30^\circ$, \mathbf{B}_{ext} causes a multiplet splitting with less than six lines, but yields either a quadruplet for $\delta = 0$ or a triplet for $\delta = \pm 30^\circ$, with an amplitude ratio of 1:2:2:1 and 2:2:2, respectively, see Figs. 3(b) and (c).

For $\mathbf{B}_{ext} \parallel c$, Eqn. (A1) is used to calculate the expected doublet frequencies (f_{calc}) with f^{ZF} from Fig. 1(c). Minimizing $|f_{calc}(\theta) - f_{exp}(\theta)| + |f_{calc}(-\theta) - f_{exp}(-\theta)|$ yields θ values that produce excellent agreement between f_{calc} and f_{exp} for E1-E3, see Table III.

Using those θ values, Eqn. (A2) is used to investigate the $\mathbf{B}_{ext} \parallel [11\bar{2}0] \perp c$ multiplet splittings. For E1 and E2, the measured frequencies are in very good agreement with the calculated values f_{calc} for $\delta = 0$ and 30° , respectively, see Table IV. Furthermore, the amplitudes are close to the predicted 1:2:2:1 and 2:2:2 ratio. For E3, $\delta = \pm 17.5^\circ$ yields a reasonable agreement between f_{calc} and f_{exp} , assuming that the outer two lines on either sides of the resulting sextet are not resolved, but appear at their average frequency (shown in bold in Table IV) with twice the amplitude. From that, an amplitude ratio of 2:1:1:2 is expected, which is indeed observed. Considering crystal alignment and the observed frequencies and amplitude ratios, we estimate the uncertainties to be $\pm 1^\circ$ for all θ values, $\pm 3.5^\circ$ for δ_{E1} and δ_{E2} , and $\pm 2^\circ$ for δ_{E3} .

Appendix B: Details on data taken in large external fields

The μ SR spectra are analyzed over the first 1 μ s [64] with the following models: Below 50 K, where f_{E2}^- and f_{E3}^- overlap, six components are considered; all three doublets share amplitude, and the overlapping line is fit to two components with the same phase and frequency, but share amplitude and relaxation rate with f_{E2}^+ and f_{E3}^+ , respectively. At and above 50 K, the data is fit to up to five exponentially damped oscillatory functions, with shared amplitudes for the E1 and E2 doublets, but separate relaxation rates.

Additionally, for the spectra at $T = 50, 110 - 155$ K, the amplitude of the E3' component, see Fig. 5, is fixed to

TABLE III. Comparison of frequencies f_{exp} measured at 2.55 K in C2, 300 G $\parallel c$, and calculated values f_{calc} , obtained with Eqn. (A1) using f^{ZF} from Fig. 1(c) and by optimizing θ to minimize $|f_{calc}(\theta) - f_{exp}(\theta)| + |f_{calc}(-\theta) - f_{exp}(-\theta)|$.

site	f^{ZF} [MHz]	f_{exp} [MHz]	f_{calc} [MHz]	θ [$^\circ$]
E1	68.53 ± 0.01	66.98 ± 0.01	66.98	-24.0
		70.28 ± 0.01	70.28	+24.0
E2	102.12 ± 0.01	101.78 ± 0.01	101.78	-6.0
		102.62 ± 0.01	102.63	+6.0
E3	76.71 ± 0.01	76.46 ± 0.03	76.46	-5.0
		77.18 ± 0.04	77.17	+5.0

TABLE IV. Comparison of frequencies f_{exp} measured at 2.2 K in C1, 200 G $\perp c$, and calculated values f_{calc} , obtained with Eqn. (A2) using f^{ZF} from Fig. 1(c), θ from Table III, φ given by $0^\circ + \delta, \pm 60^\circ + \delta, \pm 120^\circ + \delta$ and $180^\circ + \delta$ with $\delta = 0^\circ$ for E1, $\delta = 30^\circ$ for E2 and $\delta = 17.5^\circ$ for E3. Bold values correspond to the average of vertically adjacent values.

site	f^{ZF} [MHz]	θ [$^\circ$]	f_{exp} [MHz]	f_{calc} [MHz]	φ_{calc} [$^\circ$]
E1	68.52 ± 0.01	24	66.08 ± 0.03	66.05	180
			67.38 ± 0.01	67.32	± 120
			69.76 ± 0.01	69.80	± 60
			71.00 ± 0.03	71.00	0
E2	102.12 ± 0.01	6	99.80 ± 0.01	99.79	± 150
			102.16 ± 0.01	102.15	± 90
			104.45 ± 0.01	104.46	± 30
E3	76.69 ± 0.01	5	74.51 ± 0.07	74.11	+162.5
				74.42	-
				74.72	-137.5
			76.15 ± 0.09	76.15	+102.5
			77.25 ± 0.07	77.32	-77.5
				78.70	+42.5
	78.98	-			
		79.27	-17.5		

TABLE V. Comparison of frequencies f_{exp} measured at $T = 2.1$ K, $\mathbf{B}_{ext} = 4$ T $\parallel c$, and calculated values using Eqn. (A1), $f_{ext} = 541.98$ MHz, and θ values that minimize $|f_{calc}(\theta) - f_{exp}(\theta)| + |f_{calc}(-\theta) - f_{exp}(-\theta)|$. Note that 541.14 MHz is listed twice in f_{exp} , as f_{E2}^- and f_{E3}^- overlap.

site	f^{ZF} [MHz]	f_{exp} [MHz]	θ [$^\circ$]	f_{calc} [MHz]
E1	68.53	517.90 ± 0.01	-24.01	517.90
		573.26 ± 0.01	+24.01	573.30
E2	102.12	541.14 ± 0.01	-5.88	541.14
		561.62 ± 0.02	+5.88	561.71
E3	76.71	541.14 ± 0.01	-4.69	541.14
		553.54 ± 0.02	+4.69	553.56

0.0365, a value obtained by averaging over the amplitude of surrounding temperature points. This constraint is necessary in order to get a meaningful measure of the relaxation rate of this strongly damped component.

The fitted amplitudes of E1 and E2 are shown in Fig. 11(a). The temperature dependence tracks largely the ZF behavior: E2 is constant in amplitude, and E1 starts

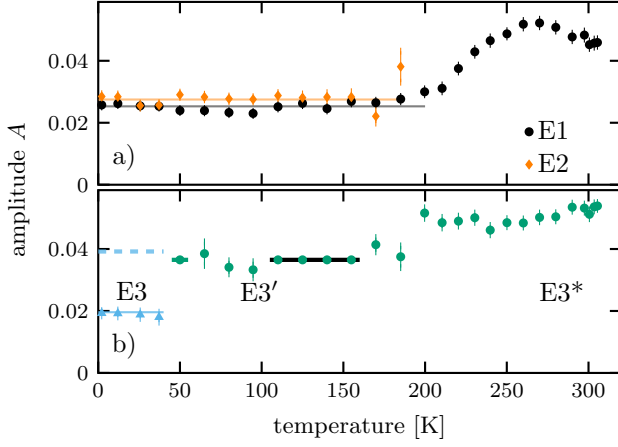


FIG. 11. Fit results for $4T||c$ spectra: amplitudes for (a) E1 and E2, and (b) for E3, E3' and E3*. The black bar indicates that the value was fixed to 0.0365.

to increase above 200 K. The displayed values are the amplitudes of one of the doublets; the total amplitude of muons in either E1 or E2 is twice that. The remaining amplitudes, associated with E3, E3' and E3* are displayed in Fig. 11(b). The points with a thick horizontal bar indicate temperature points where the amplitude was constrained. The E3 doublet amplitude accounts for only one of the doublets; the dashed line indicates the total (double) value for reference.

The frequencies obtained from fitting to five exponentially damped oscillatory components are shown in Table V. Using Eqn. (A1), f_{calc} is calculated for the θ value that minimizes $|f_{calc}(\theta) - f_{exp}(\theta)| + |f_{calc}(-\theta) - f_{exp}(-\theta)|$, yielding very good agreement with the data, and θ values matching closely those obtained in low field, see Table III.

The temperature dependence of f_{E1}^{\pm} and f_{E2}^{\pm} is modeled by Eqn. (A1) with θ from Table V, and an interpolated temperature dependence of $f_{E1}^{ZF}(T)$ in Fig. 1(c). $f_{E2}^{ZF}(T)$ was further approximated by scaling $f_{E1}^{ZF}(T)$ by the low temperature E2/E1 frequency ratio $f_{E2}^{ZF}/f_{E1}^{ZF}|_{2.2K} = 1.49$. The red lines in Fig. 6(c) represent the calculated doublet frequencies $f_{E1}^{\pm}(T)$ and $f_{E2}^{\pm}(T)$. There is good agreement with the data, indicating that θ is largely temperature independent. A small but consistent deviation from the predicted line is observed for the E1 doublet between 200 – 300 K, and discussed in Sec. VI.

Appendix C: Details on the E2→E1 transition

Here we describe a model for the E2→E1 transition assuming a thermally activated, exponential rate of the form $\Lambda(T) = \nu_0 \exp(-E_a/k_B T)$, where E_a and ν_0 are activation energy and attempt frequency. The following expression describes the observable signal precessing at

f_{E1} (compare [65, 66]):

$$\begin{aligned} S_{E1}(t) &= A_{E1} \cos(2\pi f_{E1} t) \\ &+ A_{E2} \int_0^t \Lambda e^{-\Lambda t'} \cos(2\pi f_{E1}(t-t') + 2\pi f_{E2} t') dt' \\ &= \mathcal{A} \cos(2\pi f_{E1} t + \Phi). \end{aligned} \quad (C1)$$

Muons starting out in E1 are described by the first term, whereas the second describes the E2→E1 transition taking into account the phase acquired while evolving in E2. For $t \gg \Lambda^{-1}$, the resultant combined amplitude \mathcal{A} and phase Φ can be expressed as

$$\mathcal{A} = \sqrt{\frac{A_{E2}^2 + 2A_{E2}A_{E1}}{\zeta(T)^2 + 1} + A_{E1}^2} \quad (C2)$$

$$\Phi = -\arctan \left[\frac{A_{E2}\zeta(T)}{A_{E2} + A_{E1}(1 + \zeta(T)^2)} \right], \quad (C3)$$

where

$$\zeta(T) = \frac{2\pi[f_{E1}(T) - f_{E2}(T)]}{\nu_0 \exp(-E_a/k_B T)}. \quad (C4)$$

The expressions above assume that \mathbf{B}_{int} in E1 and E2 are parallel and perpendicular to the initial spin polarization \mathbf{P}_i . In order to compare this model to data taken in both ZF and large \mathbf{B}_{ext} , small modifications, outlined below, are necessary.

In general, \mathbf{B} is not perpendicular to the initial polarization \mathbf{P}_i , causing the component of $\mathbf{B}||\mathbf{P}_i$ to act as a holding field. The polarization signal can be decomposed into oscillating and non-oscillating components [1]

$$S(t) \propto \cos(\theta)^2 \cos(\gamma\mu|\mathbf{B}|t) + \sin(\theta)^2, \quad (C5)$$

where $90^\circ - \theta$ is the angle enclosed by \mathbf{B} and \mathbf{P}_i .

Zero field. Here, $\mathbf{P}_i||c$, and for both E1 and E2, the internal field \mathbf{B}_{int} encloses an angle θ with the c -plane, see Table III. Thus $\mathbf{B}_{int} \cdot \mathbf{P}_i \neq 0$, resulting in a non-oscillatory signal component. The oscillatory f_{E1} signal amplitude represents only a fraction of $\cos(\theta_{E1} = 24^\circ)^2 = 0.83$ of muons in E1, while for E2, $\cos(\theta_{E2} = 6^\circ)^2 = 0.99$, and virtually the complete E2 component is oscillating. Thus if the complete E2 component with observed amplitude A_{E2} coherently transfers to E1, the transferred amplitude observed at f_{E1} is only $(\cos(\theta_{E1})/\cos(\theta_{E2}))^2 A_{E2}$. Strictly, this is only valid for $\Lambda^{-1} \ll 1/f_{E2}$; furthermore, a change $\Delta\varphi = 30^\circ$ of the internal field direction upon transition is neglected. A calculation addressing both issues was carried out and yielded slight improvements but no major deviations from the simple model, and was not included for clarity. The temperature dependence of $f_{E1}^{ZF}(T)$ and $f_{E2}^{ZF}(T)$ is obtained by interpolating f_{E1}^{ZF} shown in Fig. 1(c).

High field. As $\mathbf{B}_{ext} \perp \mathbf{P}_i > \mathbf{B}_{int}$, the resultant internal field is in good approximation perpendicular to \mathbf{P}_i . \mathbf{B}_{ext} causes a frequency splitting, see Section III C. The doublet frequencies, compare red lines in Fig. 6,

are given by Eqn. (A1). Here, only transitions without sign change of θ , i.e. $f_{E2}^+ \rightarrow f_{E1}^+$ and $f_{E2}^- \rightarrow f_{E1}^-$, are considered. Note that the phase shift Φ has opposite direction for the two doublet frequencies due to a sign change of ζ , see Eqns. (C3) and (C4). The model predicts slightly different temperature dependences $\mathcal{A}(T)$ for the $f_{E2}^+ \rightarrow f_{E1}^+$ and $f_{E2}^- \rightarrow f_{E1}^-$ transitions. Since the experimental frequency doublet was fit to a common amplitude, the model curve shown in Fig. 7(b) is the average of both contributions.

For a quantitative analysis, the following parameters (as obtained in the Sections above) were used: in ZF, $A_{E1} = 0.082$ and $A_{E2} = 0.090$, in high field $A_{E1} = 0.0253$ and $A_{E2} = 0.0275$. The derivation of Eqns. (C2) and (C3) does not consider initial phases ($\phi_{E1} = \phi_{E2} = 0$). This was accounted for by shifting the model curves by the E1 initial phase obtained at low temperatures.

Appendix D: Details on local hopping simulation

In order to investigate the E3' component, and obtain a better understanding of the dynamic behavior over the full temperature range, a Monte Carlo simulation of the muon depolarization function in $\mathbf{B}_{ext} = 4\text{ T} \parallel c$ assuming local hopping between adjacent sites was carried out. Stopping sites were arranged on a hexagon, with the in-plane component of \mathbf{B}_{int} pointing radially outward, and the signs of θ alternating. An exponential correlation time $\tau = 1/\nu$, where ν is the average hop rate, was assumed. Polarization spectra were simulated in the range $\nu = 10^{-1} - 10^5$ MHz for 1 μs with a time step $\Delta t = 0.0001 \mu\text{s}$ and 5000 repeats, using $f_{E3} = 76.7$ MHz for $|\mathbf{B}_{int}|$, $\theta = \pm 4.69^\circ$, and $f_{ext} = 541.98$ MHz. Details on the general setup of the simulation can be found in Ref. 67. The simulated spectra were fit to either a single oscillatory component, Eqn. (1), for fast hopping, or to two oscillatory components with shared relaxation rate in the quasi-static regime. The resulting precession frequencies and relaxation rates are shown in Fig. 12(a) and (b).

For direct comparison, the simulation results are mapped onto the data assuming an Arrhenius-like activation $T = E_b / (k_B \ln[\nu_0/\nu])$, where E_b is an activation energy and ν_0 an attempt frequency. Fig. 12, displaying in red the experimental 4 T E3/E3'/E3* (c) frequencies and (d) relaxation rate, alongside the simulation results for $\nu_0 = 5 \times 10^5$ MHz and $E_b = 42$ meV, shows excellent qualitative agreement. The E3' component is clearly identified as f_{E3}^{avg} , compare Fig. 6(c). Note that due to the approximation of a fixed internal field, and neglect of susceptibility contributions, the model loses validity with increasing temperature. Both at the low and high temperature end of the data, the relaxation rate is not well described, indicating that a simple Arrhenius activation model is insufficient to fully describe the data.

Overall, local hopping describes the E3/E3'/E3* signals in the combined data set taken in ZF, small and

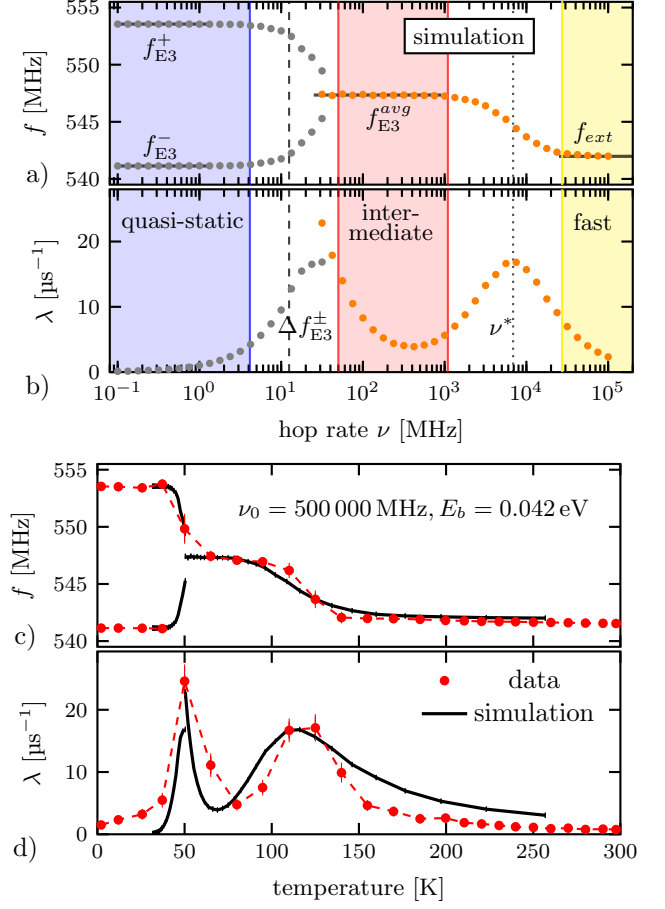


FIG. 12. Simulation of (a) precession frequencies and (b) relaxation rate assuming hopping between adjacent muon sites arranged on a hexagon in 4 T, described by an exponential correlation time $\tau = 1/\nu$, where ν is the average hop rate. There are three different regimes: quasi-static (low hop rate), where the E3 doublet is observed, intermediate hop rates, where the average of the E3 doublet is observed, and fast hopping, where internal fields are completely averaged out and a component at f_{ext} is predicted. (c) and (d): Projection of the simulated values with an Arrhenius activation relation onto the obtained E3/E3'/E3* frequencies and relaxation rate. There is excellent qualitative agreement between the model and the data (see text for details).

large \mathbf{B}_{ext} very well. There is convincing evidence that E3* arises from muons undergoing thermally activated hopping between adjacent E3 sites, causing \mathbf{B}_{int} to average to zero. This is strongly supported by the observation of E3' in large \mathbf{B}_{ext} and its identification as f_{E3}^{avg} . Additionally, the energy barrier $E_b = 42 \pm 5$ meV between sites is estimated.

Appendix E: Details on DFT calculations

DFT calculations were carried out using the Vienna ab initio Simulation Package (VASP) Version 5.4.4 [39–41].

The positive muon was modeled as a hydrogen nucleus, embedded within an 80-atom $2 \times 2 \times 2$ rhombohedral supercell (SC) of Cr_2O_3 . The local spin density approximation as parameterized by Perdew and Zunger [68] with an additional Hubbard-like correction (LDA+U) was used. The LDA+U correction scheme of Dudarev *et al.* [69] was employed with a U_{eff} of 4 eV applied to the Cr d states. This choice of U_{eff} was found to provide a good description of the crystal and electronic structure of Cr_2O_3 and is in line with values used in previous works [70]. Brillouin zone integrations were performed, using the tetrahedron method with Blöchl corrections, on a Γ -centred $4 \times 4 \times 4$ Monkhorst-Pack grid [71] for the $2 \times 2 \times 2$ SC. A plane-wave cutoff of 700 eV was used. With respect to a 900 eV cutoff and an $8 \times 8 \times 8$ k -point mesh, en-

ergy differences were found to be converged to within 1 meV/formula unit and forces to within 3 meV/Å. The full convergence tests are available in the Supplemental Information [27]. Within the projector-augmented plane-wave (PAW) method [72, 73], the 14 electrons for Cr ($3s^2 3p^6 3d^4 4s^2$) and 6 for O ($2s^2 2p^4$) were treated explicitly [74]. A collinear treatment of spins was adopted and the well established ‘+ – + –’ G-type antiferromagnetic order, indicated in the inset of Fig. 1, confirmed. Spin-orbit coupling has previously been found to be negligible in Cr_2O_3 [70] and was therefore not included here. Supercells of up to $4 \times 4 \times 4$ were tested in order to ensure that the imposed periodic boundary conditions did not introduce artifacts. In particular, we found negligible changes in the calculated contact and dipole contributions with respect to the results shown in Table II.

-
- [1] A. Yaouanc and P. Dalmas de Réotier, *Muon Spin Rotation, Relaxation, and Resonance* (Oxford University Press, 2011).
- [2] K. Chow, B. Hitti, and R. Kiefl, in *Semiconductors and Semimetals*, Vol. 51 (Elsevier, 1998) pp. 137–207.
- [3] S. F. J. Cox, J. S. Lord, S. P. Cottrell, J. M. Gil, H. V. Alberto, A. Keren, D. Prabhakaran, R. Scheuermann, and A. Stoykov, *J. Phys. Condens. Matter* **18**, 1061 (2006).
- [4] S. F. J. Cox, J. L. Gavartin, J. S. Lord, S. P. Cottrell, J. M. Gil, H. V. Alberto, J. P. Duarte, R. C. Vilão, N. A. de Campos, D. J. Keeble, E. A. Davis, M. Charlton, and D. P. van der Werf, *J. Phys. Condens. Matter* **18**, 1079 (2006).
- [5] S. F. J. Cox, *Rep. Prog. Phys.* **72**, 116501 (2009).
- [6] Y. J. Uemura, R. Keitel, M. Senba, R. F. Kiefl, S. R. Kretitzman, D. R. Noakes, J. H. Brewer, D. Harshman, E. J. Ansaldo, K. M. Crowe, A. M. Portis, and V. Jaccarino, *Hyperfine Interact.* **31**, 313 (1986).
- [7] H. A. Jahn and E. Teller, *Proc Roy Soc A* **161**, 16 (1937).
- [8] T. Holstein, *Ann. Phys.* **8**, 325 (1959).
- [9] H. Nickisch, H. Thomas, and K.-H. Höck, *Birkhäuser* (1983).
- [10] I. E. Dzyaloshinskii, *Sov Phys JETP* **10**, 628 (1960).
- [11] D. N. Astrov, *Sov Phys JETP* **13**, 729 (1961).
- [12] G. T. Rado and V. J. Folen, *Phys. Rev. Lett.* **7**, 310 (1961).
- [13] H. Wiegmann, A. G. M. Jansen, P. Wyder, J.-P. Rivera, and H. Schmid, *Ferroelectrics* **162**, 141 (1994).
- [14] M. Fiebig, *J. Phys. Appl. Phys.* **38**, R123 (2005).
- [15] Q. N. Meier, M. Fechner, T. Nozaki, M. Sahashi, Z. Salman, T. Prokscha, A. Suter, P. Schoenherr, M. Lilienblum, P. Borisov, I. E. Dzyaloshinskii, M. Fiebig, H. Luetkens, and N. A. Spaldin, *Phys. Rev. X* **9** (2019).
- [16] P. Borisov, A. Hochstrat, X. Chen, W. Kleemann, and C. Binek, *Phys. Rev. Lett.* **94** (2005).
- [17] X. He, Y. Wang, N. Wu, A. N. Caruso, E. Vescovo, K. D. Belashchenko, P. A. Dowben, and C. Binek, *Nat. Mater.* **9**, 579 (2010).
- [18] T. Kosub, M. Kopte, R. Hühne, P. Appel, B. Shields, P. Maletinsky, R. Hübner, M. O. Liedke, J. Fassbender, O. G. Schmidt, and D. Makarov, *Nat. Commun.* **8**, 13985 (2017).
- [19] D. I. Khomskii, *Nat. Commun.* **5**, 4793 (2014).
- [20] K. Rüegg, C. Boekema, W. Hofmann, W. Kündig, and P. F. Meier, *Hyperfine Interact.* **6**, 99 (1979).
- [21] K. Rüegg, C. Boekema, A. Denison, W. Hoffmann, and W. Kündig, *J. Magn. Magn. Mater.* **15-18**, 669 (1980).
- [22] C. Boekema, K. Rüegg, and W. P. Hofmann, *Hyperfine Interact.* **8**, 609 (1981).
- [23] C. Boekema, A. B. Denison, and K. J. Rüegg, *J. Magn. Magn. Mater.* **36**, 111 (1983).
- [24] A. Suter and B. Wojek, *Phys. Procedia* **30**, 69 (2012).
- [25] A. B. Denison, *J. Appl. Phys.* **55**, 2278 (1984).
- [26] E. Holzschuh, A. B. Denison, W. Kündig, P. F. Meier, and B. D. Patterson, *Phys. Rev. B* **27**, 5294 (1983).
- [27] This measurement with $\mathbf{B}_{\text{ext}} = 300 \text{ G} \parallel c$ was taken in the Omni-Prime spectrometer. The Fourier transform is shown over the time range of 0.1 – 2 μs .
- [28] E. Samuelsen, M. Hutchings, and G. Shirane, *Physica* **48**, 13 (1970).
- [29] A. M. Browne and A. M. Stoneham, *J. Phys. C Solid State Phys.* **15**, 2709 (1982).
- [30] A. M. Stoneham, *Hyperfine Interact.* **17**, 53 (1984).
- [31] H. Graf, W. Hofmann, W. Kündig, P. F. Meier, B. D. Patterson, W. Reichhart, and A. Rodriguez, *Hyperfine Interact.* **4**, 452 (1978).
- [32] V. N. Duginov, V. G. Grebinnik, K. I. Gritsaj, T. N. Mamedov, V. G. Olshevsky, V. Y. Pomjakushin, V. A. Zhukov, B. F. Kirillov, I. A. Krivosheev, A. V. Pirogov, and A. N. Ponomarev, *Hyperfine Interact.* **85**, 317 (1994).
- [33] A. Amato, D. Andreica, F. Gygax, M. Pinkpank, N. Sato, A. Schenck, and G. Solt, *Phys. B Condens. Matter* **289-290**, 447 (2000).
- [34] A. M. Mulders, P. C. M. Gubbens, C. Kaiser, A. Amato, F. Gygax, A. Schenck, P. Dalmas de Réotier, A. Yaouanc, K. Buschow, F. Kayzel, and A. Menovsky, *Hyperfine Interact.* **133**, 197 (2001).
- [35] J. W. Schneider, R. F. Kiefl, K. Chow, S. F. J. Cox, S. A. Dodds, R. C. DuVarney, T. L. Estle, R. Kadono, S. R. Kretitzman, R. L. Lichti, and C. Schwab, *Phys. Rev. Lett.* **68**, 3196 (1992).
- [36] P. Bonfà and R. De Renzi, *J. Phys. Soc. Jpn.* **85**, 091014 (2016).

- [37] I. J. Onuorah, P. Bonfà, and R. De Renzi, *Phys. Rev. B* **97** (2018).
- [38] I. J. Onuorah, P. Bonfà, R. De Renzi, L. Monacelli, F. Mauri, M. Calandra, and I. Errea, *Phys. Rev. Materials* **3**, 073804 (2019), arXiv:1904.11913.
- [39] G. Kresse and J. Hafner, *Phys. Rev. B* **47**, 558 (1993).
- [40] G. Kresse and J. Hafner, *Phys. Rev. B* **49**, 14251 (1994).
- [41] G. Kresse and J. Furthmüller, *Phys. Rev. B* **54**, 11169 (1996).
- [42] See Supplemental Information at DOI:10.5281/zenodo.3378994.
- [43] R. C. Vilão, R. B. L. Vieira, H. V. Alberto, J. M. Gil, A. Weidinger, R. L. Lichti, B. B. Baker, P. W. Mengyan, and J. S. Lord, *Phys. Rev. B* **92** (2015).
- [44] K. Shimomura, R. Kadono, A. Koda, K. Nishiyama, and M. Mihara, *Phys. Rev. B* **92** (2015).
- [45] D. Emin, *Phys. Today* **35**, 34 (1982).
- [46] C. G. Van de Walle, *Phys. Rev. Lett.* **85**, 1012 (2000).
- [47] R. F. Kiefl, M. Celio, T. L. Estle, S. R. Kretzman, G. M. Luke, T. M. Riseman, and E. J. Ansaldo, *Phys. Rev. Lett.* **60**, 224 (1988).
- [48] K. Nishiyama, *Hyperfine Interact.* **135/137**, 289 (2001).
- [49] M. Bimbi, G. Allodi, R. De Renzi, C. Mazzoli, and H. Berger, *Phys. Rev. B* **77** (2008).
- [50] V. G. Storchak, O. E. Parfenov, J. H. Brewer, P. L. Russo, S. L. Stubbs, R. L. Lichti, D. G. Eshchenko, E. Morenzoni, T. G. Aminov, V. P. Zlomanov, A. A. Vinokurov, R. L. Kallaher, and S. von Molnár, *Phys. Rev. B* **80** (2009).
- [51] R. F. Kiefl, *Phys. Rev. B* **83** (2011).
- [52] V. G. Storchak, J. H. Brewer, R. L. Lichti, T. A. Lograsso, and D. L. Schlagel, *Phys. Rev. B* **83** (2011).
- [53] A. Amato, P. Dalmas de Reotier, D. Andreica, A. Yaouanc, A. Suter, G. Lapertot, I. M. Pop, E. Morenzoni, P. Bonfà, F. Bernardini, and R. De Renzi, *Phys. Rev. B* **89** (2014).
- [54] T. Dietl and H. Ohno, *Rev. Mod. Phys.* **86**, 187 (2014).
- [55] H. Baqiah, N. Ibrahim, S. Halim, S. Chen, K. Lim, and M. A. Kechik, *J. Magn. Magn. Mater.* **401**, 102 (2016).
- [56] M. Bououdina, A. Dakhel, A. Jaafar, J. Dai, and Y. Song, *J. Alloys Compd.* **776**, 575 (2019).
- [57] C. G. Van de Walle and J. Neugebauer, *Nature* **423**, 626 (2003).
- [58] N. A. Spaldin and R. Ramesh, *Nat. Mater.* **18**, 203 (2019).
- [59] Ç. Kılıç and A. Zunger, *Appl. Phys. Lett.* **81**, 73 (2002).
- [60] S. F. J. Cox, E. A. Davis, S. P. Cottrell, P. J. C. King, J. S. Lord, J. M. Gil, H. V. Alberto, R. C. Vilão, J. Piroto Duarte, N. Ayres de Campos, A. Weidinger, R. L. Lichti, and S. J. C. Irvine, *Phys. Rev. Lett.* **86**, 2601 (2001).
- [61] P. W. Peacock and J. Robertson, *Appl. Phys. Lett.* **83**, 2025 (2003).
- [62] K. Xiong, J. Robertson, and S. J. Clark, *J. Appl. Phys.* **102**, 083710 (2007).
- [63] K. Momma and F. Izumi, *J. Appl. Crystallogr.* **44**, 1272 (2011).
- [64] A small sample misalignment of less than 1° seems to cause a further splitting of the line at times longer than $1\ \mu\text{s}$. This sub-splitting affects the various multiplet frequencies differently and has a small temperature dependence which is not fully understood. Limiting the analysis (and the depicted FT) to the first $1\ \mu\text{s}$ effectively smooths out the substructure; however a separate relaxation rate for the E1 doublet is required and attributed to broadening caused by this misalignment sub-splitting.
- [65] P. F. Meier, *Phys. Rev. A* **25**, 1287 (1982).
- [66] M. H. Dehn, D. J. Arseneau, P. Böni, M. D. Bridges, T. Buck, D. L. Cortie, D. G. Fleming, J. A. Kelly, W. A. MacFarlane, M. J. MacLachlan, R. M. L. McFadden, G. D. Morris, P.-X. Wang, J. Xiao, V. M. Zamarion, and R. F. Kiefl, *J. Chem. Phys.* **145**, 181102 (2016).
- [67] M. H. Dehn, D. G. Fleming, W. A. MacFarlane, M. J. MacLachlan, V. M. Zamarion, and R. F. Kiefl, *Proc 14th Int Conf Muon Spin Rotat. Relax. Reson. J. Phys. Soc. Jpn.* **21**, 011032 (2018).
- [68] J. P. Perdew and A. Zunger, *Phys. Rev. B* **23**, 5048 (1981).
- [69] S. L. Dudarev, G. A. Botton, S. Y. Savrasov, C. J. Humphreys, and A. P. Sutton, *Phys. Rev. B* **57**, 1505 (1998).
- [70] S. Shi, A. L. Wysocki, and K. D. Belashchenko, *Phys. Rev. B* **79** (2009).
- [71] H. J. Monkhorst and J. D. Pack, *Phys. Rev. B* **13**, 5188 (1976).
- [72] P. E. Blöchl, *Phys. Rev. B* **50**, 17953 (1994).
- [73] G. Kresse and D. Joubert, *Phys. Rev. B* **59**, 1758 (1999).
- [74] The Cr, O and H PAWs are dated: 23rd Jul. 2007, 22nd Mar. 2012 and 6th May 1998 respectively.